AGU PUBLICATIONS

JGR

Journal of Geophysical Research: Oceans

RESEARCH ARTICLE

10.1002/2014JC009992

Companion to *King et al.* [2015], doi:10.1002/2014JC009993.

Key Points:
- Second-order structure function analysis in the Tropical Pacific
- Comparison of scatterometer wind data with turbulence theory
- Turbulence scaling exponent for mesoscale ocean winds

Correspondence to:
J. Vogelzang,
jur.vogelzang@knmi.nl

Citation:
King, G. P., J. Vogelzang, and A. Stoffelen (2015), Second-order structure function analysis of scatterometer winds over the Tropical Pacific, *J. Geophys. Res. Oceans*, *120*, 362–383, doi:10.1002/2014JC009992.

Received 24 MAR 2014
Accepted 5 DEC 2014
Accepted article online 9 DEC 2014
Published online 28 JAN 2015

Second-order structure function analysis of scatterometer winds over the Tropical Pacific

Gregory P. King[1,2,3,4], Jur Vogelzang[5], and Ad Stoffelen[5]

[1]Centro de Geofisica—IDL, Campo Grande, Edificio 8, Universidade de Lisboa, Lisboa, Portugal, [2]Instituto Gulbenkian de Ciencia, Oeiras, Portugal, [3]School of Marine Sciences, Nanjing University of Information Science and Technology, Nanjing, China, [4]Institute of Marine Sciences (ICM-CSIC), Passeig Marítim Barceloneta, Barcelona, Spain, [5]Royal Netherlands Meteorological Institute, De Bilt, Netherlands

Abstract *Kolmogorov* second-order structure functions are used to quantify and compare the small-scale information contained in near-surface ocean wind products derived from measurements by ASCAT on MetOp-A and SeaWinds on QuikSCAT. Two ASCAT and three SeaWinds products are compared in nine regions (classified as rainy or dry) in the tropical Pacific between 10°S and 10°N and 140° and 260°E for the period November 2008 to October 2009. Monthly and regionally averaged longitudinal and transverse structure functions are calculated using along-track samples. To ease the analysis, the following quantities were estimated for the scale range 50 to 300 km and used to intercompare the wind products: (i) structure function slopes, (ii) turbulent kinetic energies (*TKE*), and (iii) vorticity-to-divergence ratios. All wind products are in good qualitative agreement, but also have important differences. Structure function slopes and *TKE* differ per wind product, but also show a common variation over time and space. Independent of wind product, longitudinal slopes decrease when sea surface temperature exceeds the threshold for onset of deep convection (about 28°C). In rainy areas and in dry regions during rainy periods, ASCAT has larger divergent *TKE* than SeaWinds, while SeaWinds has larger vortical *TKE* than ASCAT. Differences between SeaWinds and ASCAT vortical *TKE* and vorticity-to-divergence ratios for the convectively active months of each region are large.

1. Introduction

The ocean and atmosphere exchange heat, moisture, and momentum across the air/sea boundary through interactions with small-scale structures (i.e., <1000 km) in the near-surface winds. This exchange affects atmosphere and ocean circulations, weather, and climate. In order to improve their modeling and prediction, global measurements of near-surface ocean wind vectors at high resolution over the oceans are required. Nowadays, this can be done using scatterometers carried on orbiting satellites.

Satellite scatterometers transmit microwaves toward the Earth and measure the backscattered radiation from the wind-roughened ocean surface. Sophisticated processing results in high-quality ocean vector winds that resolve small-scale structure in the near-surface ocean wind field [*Vogelzang et al.*, 2011]. Forecasters use satellite winds in marine weather prediction, wave and surge forecasting, and the monitoring of tropical cyclones and prediction of their trajectories [e.g., *Sienkiewicz et al.*, 2010]. They are also used in numerical weather prediction (NWP) [*Isaksen and Janssen*, 2004], for driving ocean models, and to investigate climate variability in both the atmosphere and the ocean [e.g., *Bourassa et al.*, 2010].

Scatterometer wind products differ in the small-scale information they contain. Differences are mainly due to instrument design (radar frequency and observation geometry), methods used to produce wind vectors from the measured radar backscatter, quality control, and sampling. Two related spatial analysis methods that can be used to quantify the information content are wavenumber spectra and second-order structure functions. Wavenumber spectra have been studied and compared with two-dimensional turbulence theory by *Freilich and Chelton* [1986], *Wikle et al.* [1999], *Patoux and Brown* [2001], and *Xu et al.* [2011]. Spectral analysis has also been used to compare the effects of noise and processing methods on the effective resolution of winds derived from ASCAT and SeaWinds [*Vogelzang et al.*, 2011]. While spectral analysis can lead to significant results in certain study cases, it has limitations—the principle one being that it cannot be applied if samples have too many missing points. Missing points arise from instrument outage or because the

retrieved wind is of low quality (mainly due to radar signal contamination caused by extreme wind variability, rain, land, or ice). *Vogelzang et al*. [2011] show that from all ASCAT wind data at 25 km grid size in January 2009 only 6% is used in a spectral analysis. This increases to 35% when isolated missing points are interpolated over, leaving about two thirds of the data unused.

Structure functions were introduced by *Kolmogorov* [1941] and are the key tool used to test turbulence theory predictions in laboratory experiments and numerical simulations [cf., *Sreenivasan and Antonia*, 1997]. In this paper, we use second-order structure functions to analyze ocean vector winds derived from the Advanced Scatterometer (ASCAT) onboard the MetOp-A satellite and the SeaWinds scatterometer onboard the QuikSCAT satellite. Missing points are much less a problem in a structure function analysis. Indeed the structure function calculation uses all valid data contained in each sample. This yields more representative statistics and also facilitates investigation of rainy areas and regions of limited size.

The analysis is carried out for a period when both scatterometers were operational (November 2008 to October 2009) and focuses on the climatically important Tropical Pacific, subdivided into rainy and dry regions. The rainy regions contain convergence zones and pools of very warm water that give rise to deep convection and heavy rain throughout the year, while the dry regions contain the east Pacific cold tongue and have little rain. The impact of rain contamination is small for ASCAT, but large for SeaWinds. Consequently, rain contamination causes much SeaWinds data to be rejected over the rainy tropics, making this region particularly difficult to study using spectral methods.

We study ASCAT wind products and SeaWinds products at two different grid sizes (12.5 and 25 km); all products are level 2B swath winds produced from orbit data. Scatterometers differ in their radar frequency, observation geometry, and sampling. Products differ in spatial aggregation of the radar backscatter, wind retrieval processing, and quality control. The two ASCAT products are both operational near-real-time products. The three SeaWinds products are: (i) a near-real-time product at 25 km; (ii) a reprocessing of the real-time product using different wind retrieval algorithms and quality control; and (iii) a science data product at 12.5 km: QuikSCAT version 3 L2B, which contains many algorithm improvements [*Fore et al*., 2013]. The differences in the three SeaWinds products allow some investigation of different quality control and spatial processing on the statistics.

The paper is organized as follows. Section 2 contains the basic definitions and formulas for the second-order structure function and its relationship to the autocorrelation function and spectrum. Theoretical relationships derived for homogeneous, isotropic turbulence are summarized. Section 3 describes the ASCAT and SeaWinds scatterometers, lists and briefly describes the wind products and their processing. Section 4 describes the main geophysical features in the Tropical Pacific affecting ocean winds and justifies the regional subdivision using rain-rates measured by the Tropical Rain Measuring Mission. The results show that all wind products are in qualitative agreement. Quantitatively there are some important differences, the most obvious being (i) different scaling laws per wind product and (ii) in rainy areas and in dry regions during rainy periods ASCAT has larger divergent turbulent kinetic energy (*TKE*), while SeaWinds has larger vortical *TKE*. Our conclusions are given in section 6.

2. Second-Order Structure Functions

2.1. Definitions and Limiting Values

Using the mathematical framework of random functions and physical hypotheses based on Richardson's concept of an energy cascade (eddies breaking up into smaller eddies), *Kolmogorov* [1941] introduced the velocity increment probability distribution and its moments (structure functions). Velocity increments are useful because they emphasize the effects of scales of the order of the separation r. Two-point statistics with respect to the increments at scale r are given by the PDF $P_r(\delta\mathbf{u})$, where $\delta\mathbf{u}=(\delta u_L, \delta u_{1T}, \delta u_{2T})$, $\delta u_L = u_L(x+r) - u_L(x)$, and $\delta u_{iT} = u_{iT}(x+r) - u_{iT}(x)$. The subscript L indicates the longitudinal component and T the transverse component, respectively, the components parallel and perpendicular to the coordinate x along which increments are taken. In 3-D isotropic turbulence, the two transverse directions are statistically equivalent, so that $\delta u_T = \delta u_{1T} = \delta u_{2T}$. The second-order structure functions are defined by

$$D_{LL}(r) = \langle \delta u_L \delta u_L \rangle, \tag{1a}$$

$$D_{TT}(r)=\langle \delta u_T \delta u_T \rangle, \tag{1b}$$

$$D_{LT}(r)=\langle \delta u_L \delta u_T \rangle=0, \tag{1c}$$

with $\langle . \rangle$ denoting an ensemble average, $\langle \delta u_L(r) \rangle = \langle \delta u_T(r) \rangle = 0$, and (1c) follows from the assumption of isotropy.

Assuming homogeneity and noise-free data, D_{LL} and D_{TT} can be written in terms of the variances σ_L^2, σ_T^2, and autocorrelation functions $\rho_L(r)$, $\rho_T(r)$ of velocities u_L, u_T as

$$D_{jj}(r)=2\sigma_j^2\left(1-\rho_j(r)\right), \tag{2}$$

where $j=L, T$. At large distances, when the autocorrelations go to zero,

$$\lim_{r\to\infty} D_{jj}(r)=2\sigma_j^2. \tag{3}$$

At $r=0$, $\rho_L(0)=\rho_T(0)=1$, so that

$$D_{LL}(0)=D_{TT}(0)=0. \tag{4}$$

2.2. Relationship With the Energy Spectrum

The energy spectrum and second-order structure function are in Fourier duality. Setting $j=L$ in Eq. (2) and taking the Fourier transform yields the *extended Wiener-Khinchin* formula [cf., *Frisch*, 1995]:

$$D_{LL}(r)=2\int_0^\infty dk(1-\cos kr)E_L(k), \tag{5}$$

where E_L is the one-dimensional longitudinal spectral energy density at wavenumber k.

2.2.1. Power Laws

If structure functions and energy spectra follow power laws $D_{LL}(r) \propto r^\gamma$ and $E_L(k) \propto k^{-\mu}$, then if $0 < \gamma < 2$, the exponents are related by $\mu=\gamma+1$ [cf., *Frisch*, 1995]. *Nastrom et al.* [1984] found that turbulence near the tropopause was to a good approximation described from about 2 to 400 km by the Kolmogorov $k^{-5/3}$ power law, and from about 600 to 2000 km by the geostrophic turbulence k^{-3} power law. In terms of structure functions, these correspond, respectively, to $r^{2/3}$ and r^2 power laws [see *Lindborg*, 1999; *Frehlich and Sharman*, 2010].

2.2.2. Turbulent Kinetic Energy

The turbulent kinetic energy contained in scales less than r can be estimated from spectra by integration

$$TKE_j(r) \propto \int_{2\pi/r}^\infty dk E_j(k), \tag{6}$$

or from the structure function

$$TKE_j(r) \propto D_{jj}(r). \tag{7}$$

The two estimates are not equal. However, Vogelzang et al. (J. Vogelzang, G. P. King, and A. Stoffelen, Spatial variances and their relation to second-order structure functions and spectra, submitted to *Journal of Geophysical Research*, 2014) show that for the ocean surface winds over the tropical Pacific, to a good approximation $TKE_j(r) \approx \frac{1}{5} D_{jj}(r)$.

2.3. Isotropy Relation and Vorticity-to-Divergence Ratio

If the turbulence is incompressible, then D_{LL} and D_{TT} are related by the isotropy relation [cf. *Frisch*, 1995], which can be written for d-dimensional turbulence as

$$D_{TT}(r)=D_{LL}(r)+\frac{r}{d-1}\frac{\mathrm{d}}{\mathrm{d}r}D_{LL}(r). \tag{8}$$

It follows from (8) that if $D_{LL}(r) \sim r^{2/3}$, then $D_{TT}(r) \sim r^{2/3}$.

Note that at small r, $\delta u_L \approx r(\partial u_L/\partial x)$ and $\delta u_T \approx r(\partial u_T/\partial x)$. Thus $D_{LL}(r)$ represents the divergent energy, $D_{TT}(r)$ the shear or vortical energy, and their ratio

$$R(r)=D_{TT}(r)/D_{LL}(r), \tag{9}$$

represents the ratio of vorticity-to-divergence. Again if $D_{LL}(r) \sim r^{2/3}$, then it follows from (8) that $R=(3d-1)/(3d-3)$, yielding $R=5/3$ for 2-D turbulence, and $R=4/3$ for 3-D turbulence. On the other hand, if turbulence is due to gravity wave interactions, then $R=3/5$ [*Lindborg*, 2007]. Finally, we note that in the case of geostrophic turbulence, substituting $D_{LL}(r) \sim r^2$ into (8) yields $R=3$. Thus, turbulence in the atmosphere can be considered to be dominated by vortical modes if $R > 1$ or dominated by divergent modes if $R < 1$.

3. Data

3.1. Satellites and Scatterometer

The QuikSCAT satellite was launched by the National Aeronautics and Space Administration (NASA) in June 1999. The mission produced ocean vector winds from July 1999 until November 2009. The MetOp-A satellite was launched in October 2006 and is operated by the European Organisation for the Exploitation of Meteorological Satellites (EUMETSAT). Both satellites are in quasi-sun-synchronous orbits with an inclination angle $\theta=98.6^o$. The local equator crossing times are about 06:30 (ascending) and 18:30 (descending) for QuikSCAT, and about 09:30 (descending) and 21:30 (ascending) for MetOp-A.

The SeaWinds-on-QuikSCAT scatterometer transmits at Ku-band (13.4 GHz) and has a rotating pencil-beam design with an 1800 km wide swath [*Tsai et al*., 2000]. The pencil-beam design has a complicated observation geometry that varies across the swath (due to the changing azimuth angle of the observations with respect to the satellite ground track), resulting in a varying performance that is reduced in the nadir region and far swath. The ASCAT-on-MetOp-A scatterometer transmits at C-band (5.3 GHz) and has a dual-swath fan-beam configuration with two 550 km wide swaths separated by a nadir gap of about 700 km [*Figa-Saldaña et al*., 2002]. The fan-beam configuration ensures a fixed observation geometry in terms of azimuth, but the look angle of the observations varies across the swath.

3.2. Processing Steps

Instrument power measurements are calibrated, converted to normalized radar cross-section, and spatially aggregated. This process involves averaging individual backscatter measurements and resampling them into an along-track, cross-track swath grid of wind vector cells (WVCs) for wind retrieval [*Figa-Saldaña et al*., 2002; *Hoffman and Leidner*, 2005; *Dunbar et al*., 2006]. The true spatial resolution of the wind field is about twice the grid size. Such oversampling by a factor of two is common in radar applications.

The next level of processing carries out wind retrieval, ambiguity removal, and quality control. Wind retrieval involves an inversion step [*Stoffelen and Portabella*, 2006] followed by a spatial filtering procedure for ambiguity removal [*Stiles et al*., 2002; *Stoffelen et al*., 2000]. The inversion step employs an empirically derived geophysical model function (GMF) to relate backscatter, obtained in the local observation geometry, to the equivalent neutral-stability vector wind at a height of 10 meters. Due to the nature of radar backscatter from the ocean surface, this procedure usually provides multiple solutions referred to as ambiguities. An ambiguity removal algorithm, imposing spatial constraints, is applied to produce a spatially consistent field of winds, selected from the solution sets provided at each WVC.

Quality control procedures include checking that there is enough good data for wind retrieval, and flags a WVC if the signal is corrupted by the presence of land, ice, rain or when the retrieved wind vector is inconsistent with the GMF.

3.3. Wind Products

The following wind products are compared in this paper:

ASCAT-12.5 and *ASCAT-25*: Spatial aggregation of radar cross-section data was carried out by EUMETSAT to 12.5 and 25 km WVCs, respectively. The cross-section data are calculated by resampling measurements, through spatial averaging individual backscatter measurements. The weighting function chosen for the averaging is a two-dimensional Hamming window, designed to provide noise reduction [*Figa-Saldaña et al*., 2002]. Wind retrieval is carried out at the Royal Netherlands Meteorological Institute (KNMI) using the ASCAT Wind Data Processor (AWDP; www.knmi.nl/scatterometer). The GMF used in the AWDP is CMOD5.n

[*Portabella and Stoffelen*, 2009] and ambiguity removal is carried out using a two-dimensional variational method (2DVAR) [*Vogelzang et al*., 2009].

SeaWinds-NOAA is a near-real-time product on a 25 km grid that was issued by the National Oceanic and Atmospheric Administration (NOAA) and is described in detail by *Hoffman and Leidner* [2005]. Spatial aggregation uses a centroid binning method that assigns a backscatter slice to only one WVC; all backscatter slices of the same azimuth and polarization in a WVC are averaged into one value before the wind retrieval. The GMF is QSCAT-1 and the spatial filtering for ambiguity removal is carried out using a median filter followed by a sophisticated algorithm called Direction Interval Retrieval with Thresholded Nudging (DIRTH) [*Stiles et al*., 2002]. Rain-flagging is carried out using the MUDH algorithm [cf. *Weissman et al*., 2012].

SeaWinds-KNMI is a reprocessing of SeaWinds-NOAA cross-section data by KNMI using improved (rain) quality control [*Portabella and Stoffelen*, 2002]. The spatial aggregation and WVC grid size (25 km) is the same as for SeaWinds-NOAA. The GMF is NSCAT-2, and the retrieved ambiguous wind vector PDF is fully represented in the 2DVAR ambiguity removal by using the Multiple Solution Scheme (MSS) [*Portabella and Stoffelen*, 2004] resulting in high quality winds [*Vogelzang et al*., 2009, 2011]. *Ebuchi* [2013] evaluated this processing applied to the very similar OceanSat-2 scatterometer.

QSCAT-12.5 (version 3) is the recently released science data product on a 12.5 km grid produced by the NASA Jet Propulsion Laboratory (JPL). It is the result of reprocessing the entire SeaWinds on QuikSCAT data set with many algorithm improvements [*Fore et al*., 2013]. Spatial aggregation uses an overlap binning method that increases the number of backscatter slices being assigned to the same WVC. The GMF is Ku2011 and ambiguity removal is carried out using a median filter followed by an improved DIRTH algorithm. Rain-flagging is carried out using the IMUDH algorithm [cf., *Weissman et al*., 2012].

Collocated NWP forecasts interpolated in space and time to the scatterometer grid are packaged with each product in the original data set. The SeaWinds-NOAA and QSCAT products are collocated with NWP forecasts from the National Center for Environmental Prediction (NCEP) model. The ASCAT and SeaWinds-KNMI products are collocated with NWP forecasts from the European Centre for Medium range Weather Forecasting (ECMWF) model.

3.4. Spatial Processing Differences

Spatial processing of the radar backscatter affects the spatial statistics. The most important differences in processing that are expected to affect spatial statistics are:

i. *Backscatter averaging*. Backscatter data are averaged locally and the fundamental footprints extend the averaging box (i.e., WVC). This implies spatial filtering and noise reduction, but also causes signal to be lost. Different local spatial filtering of backscatter data thus causes signal and noise changes. For ASCAT, the differences between collocated winds obtained from box-car and Hamming filtered backscatter data over open sea have been reviewed and found negligible [*Verhoef and Stoffelen*, 2013].

ii. *Scatterometer geometry and related ambiguity removal filtering (AR)*. ASCAT (and its forerunner ERS scatterometer) inversion generally provides two opposing solutions as input to the AR, from which AR may select one without much spatial compromise; it is estimated that in $<$0.5% of cases selection errors occur [*Stoffelen et al*., 2000]. On the other hand, for QuikSCAT the ambiguous solutions can be noisy, skew, and broad, such that either the full wind vector PDF (MSS) [*Portabella and Stoffelen*, 2004] or solutions in wind direction windows are used at each WVC (DIRTH) [*Stiles et al*., 2002]. QuikSCAT AR uses many wind directions to select from, which obviously requires more complex spatial filtering than for ASCAT [*Portabella and Stoffelen*, 2004]. Imposing spatial constraints to produce a spatially consistent field of winds from the solution (window) sets provided at each WVC suppress the effect of the noisy, skew, and broad minima appearing in QuikSCAT retrievals, but may affect the physical integrity of the local information contained in the local backscatter fields. The subsequent filtering artifacts have been shown in spatial maps [*Stoffelen et al*., 2008], spectral analysis, and buoy validations [*Vogelzang et al*., 2011].

iii. *Rain contamination*. Rain affects the radar backscatter measured by scatterometers in several ways [*Weissman et al*., 2012]. The higher the radar frequency, the larger the impact rain has on wind retrieval. As a result, rain is a larger source of error for winds derived from Ku-band instruments (SeaWinds) than from C-band instruments (ASCAT). At Ku-band, the backscatter from the rain is approximately the same for all observing angles. As a result, there is a tendency for wind vectors retrieved in heavy rain to be aligned in

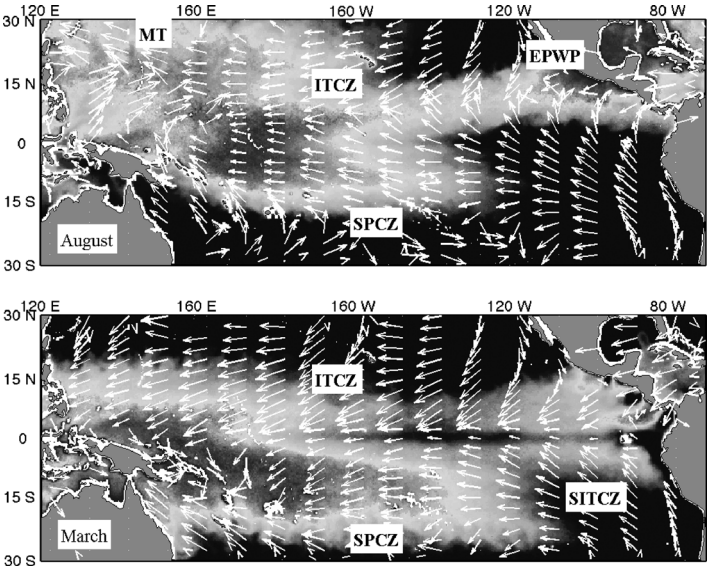

Figure 1. Sea surface temperatures and monthly ocean winds in the Tropical Pacific in (top) August and (bottom) March. Labels identify the East Pacific Warm Pool (EPWP) and the major convergence zones: Monsoon Trough (MT), Inter-Tropical Convergence Zone (ITCZ), South Pacific Convergence Zone (SPCZ), and Southern-ITCZ (SITCZ).

the cross-track direction (just as a wind blowing across the swath). Due to the way the median filter works, this can influence wind retrievals in neighboring rain-free WVCs [*Draper and Long*, 2002]. Moreover, the more complex spatial AR may aggravate errors in rainy areas, such as over the west Pacific warm pool. In contrast, the lower ASCAT radar frequency results in winds that are much less affected by rain, although they remain sensitive to secondary effects, such as the splashing of raindrops on the surface and local wind variability (wind downbursts) when rain is heavy and wind is low. These secondary effects of rain may complicate ambiguity removal [*Portabella et al*., 2012] (W. Lin et al., ASCAT wind quality control near rain, submitted to *Transactions on Geoscience and Remote Sensing*, 2014).

Besides the main effects above, any processor setting that leads to different wind vectors, different rejections, and/or different ARs may obviously lead to modified spatial characteristics. However, all processors have been optimized to provide optimal winds at each WVC and effects of such ancillary processor settings are expected to be minor within the global context of this paper.

3.5. SST and Rain-Rates

Rain-rates and sea surface temperatures were obtained from the Tropical Rainfall Measuring Mission's (TRMM) Microwave Imager (TMI) and used to characterize the local environment. The TMI data were obtained from the Remote Sensing Systems web site (http://www.ssmi.com). SeaWinds Radiometer (SRAD) rain-rates, derived from rather coarse SeaWinds measurements of the ocean radiometric brightness temperature [*Laupattarakasem et al*., 2005], are also used.

4. Study Area and Methods

4.1. Tropical Pacific

Figure 1 shows sea surface temperatures (SST) in the Tropical Pacific between latitudes 30°S and 30°N, with monthly QuikSCAT ocean wind vectors (obtained from the Remote Sensing Systems web site) superimposed. The convergence zones labeled in the figure play a central role in the organization of tropical circulations and generation of tropical weather systems. The months of August (top) and March (bottom) are shown in order to identify all the main convergence zones. They are the InterTropical Convergence Zone (ITCZ), the western North Pacific Monsoon Trough (MT), the South Pacific Convergence Zone (SPCZ), and the Southern ITCZ (S-ITCZ). Also labeled is the East Pacific Warm Pool (EPWP).

The ITCZ extends across the Pacific but in the east Pacific remains north of 4°N throughout the year. As boreal summer progresses, the ITCZ migrates north, merging with the EPWP in the eastern Pacific and with the MT in the western Pacific. The axis of the MT usually emerges from east Asia in boreal summer at about 20–25°N and extends southeastward to a terminus southeast of Guam at (13°N, 145°E). Its oceanic portion shows considerable variability in position, shape, and orientation throughout the monsoon season (June–November) [*Lander*, 1996]. The area near the trough axis is a favorable region for the genesis of tropical cyclones and monsoon depressions.

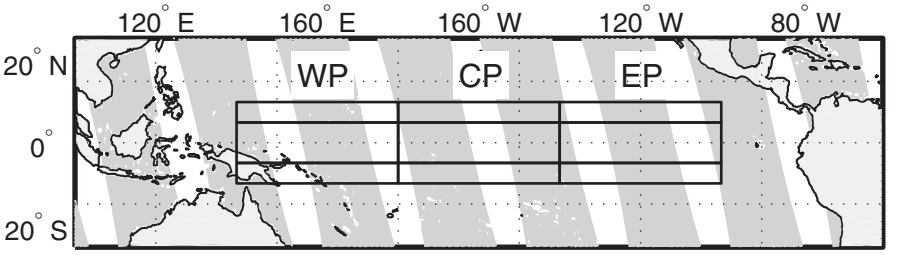

Figure 2. The boundaries of the nine geographical regions used in the present study. Nomenclature of the regions and their geographical limits are given in Table 1.

As boreal summer wanes, the ITCZ migrates southward and across the equator to merge with the SPCZ. As the ITCZ migrates southward, so too does the west Pacific warm pool, defined as the waters enclosed by the 28°C isotherm [*Wyrtki*, 1989], an empirical threshold for the onset of deep convection. The warm pool spans the western areas of the equatorial Pacific to the eastern Indian Ocean. The high SST in the warm pool creates an environment favorable to the self-organization of individual convection cells into Mesoscale Convective Systems (MCSs) with scales ~300 to 400 km [*Houze*, 2004]. These can self-organize into super-clusters ~1000–3000 km), which can in turn organize into a large-scale envelope known as the Madden-Julian Oscillation (~10,000 km).

The SPCZ is present all year, starting parallel to the equator in the western Pacific before changing direction southeastward across the Pacific. Convective activity in the SPCZ is greatest during austral summer, so that from November to April frequent and strong convective activity occurs near and just south of the equator. During boreal spring the area of strongest convergence rapidly moves northward across the equator and concentrates near the confluence of the ITCZ and MT (10–20°N) from May to October, see Figure 1 in *Zhu and Wang* [1993].

The southern boundary of the ITCZ in the east Pacific marks the location of a strong SST front that forms the northern boundary of a tongue of cool SST, known as the east Pacific cold tongue. The southern boundary of the cold tongue is formed by another strong SST front. The intensity and spatial extent of the cold tongue varies seasonally [*Mitchell and Wallace*, 1992]. During the warm season (January–June), the ITCZ is nearest the equator and the cold tongue falls to minimum intensity and spatial extent. During the wet season (typically March–April) deep convection and rain enter the region. During the cold season (July–December), the ITCZ is furthest north and the cold tongue expands, reaching maximum intensity and spatial extent in August–September.

The S-ITCZ emerges south of the equator in the east Pacific from March to April [*Masunaga and l'Ecuyer*, 2010, and references therein]. This convergence zone is caused by the deceleration of southerly surface winds as they pass over the SST front on the southern boundary of the cold tongue [*Liu*, 2002].

4.2. Study Area

The study area is shown in Figure 2 and is subdivided into three latitude bands (North, Equatorial, South) and three longitude bands (West, Central, and East Pacific). These regions isolate rainy from dry regions, as can be inferred from the latitude-time plots of monthly and zonally averaged rain-rates shown in Figure 3; also shown in that figure are monthly and zonally averaged latitude-time plots of SST. (The data for these figures were obtained from TMI data sets downloaded from the Remote Sensing Systems web site.) The nomenclature and latitude-longitude limits of the regions are given in Table 1.

4.3. Methods

The wind vectors used in this study are the most likely ("selected") solutions obtained from the processing procedure applied to each wind product. Samples were selected along-swath: WVCs in the same sample all have the same cross-swath index. Each sample was checked to ensure that only those WVCs falling inside the region of interest were used. For SeaWinds-NOAA and QSCAT-12.5, rain-flagged WVCs were flagged missing (filtered out) of the calculations. For SeaWinds-KNMI and ASCAT, wind vectors were filtered out if the KNMI quality control flag or the variational quality control flag was set [*KNMI*, 2006, 2013]. Samples from both the ascending and descending passes of the satellite and from the whole swath (including the outer

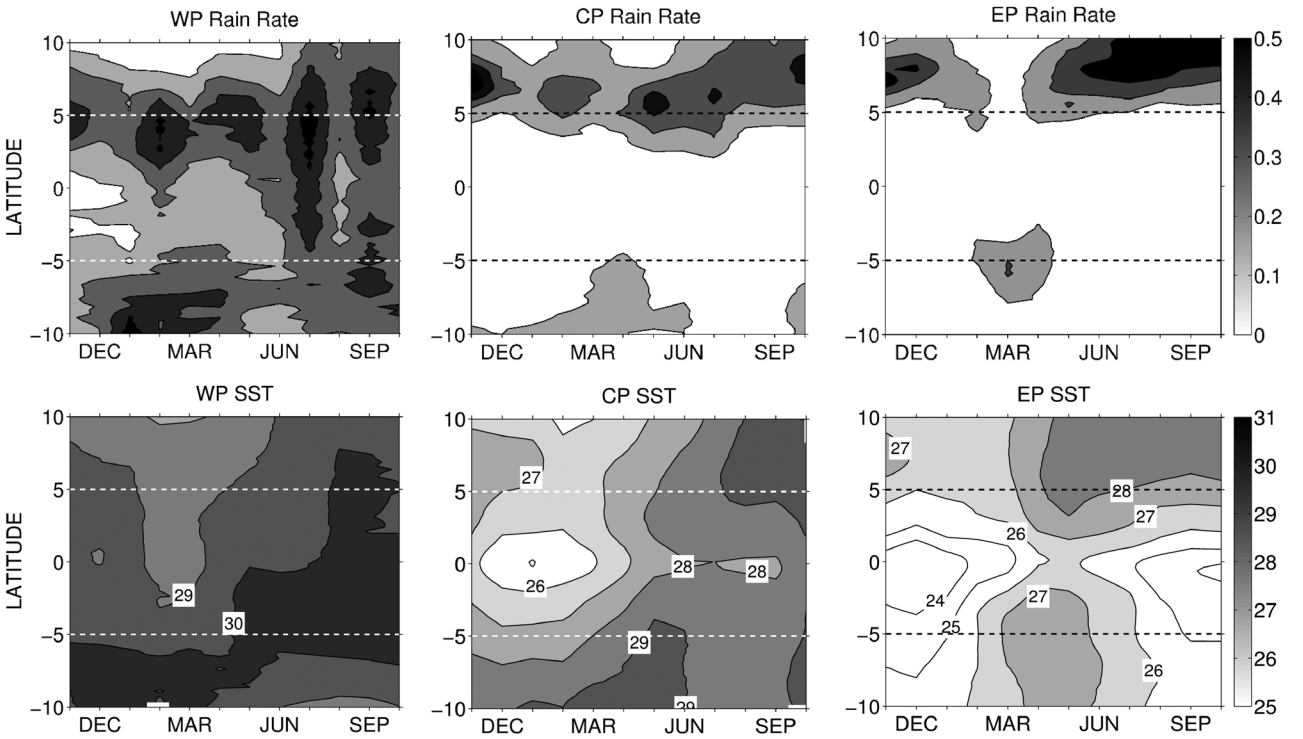

Figure 3. Latitude-time plots of monthly and zonally averaged (top) rain-rates and (bottom) sea surface temperatures measured by the TRMM Microwave Imager (TMI) during the study period.

and nadir parts of the SeaWinds swath) were used to construct velocity increment PDFs and calculate structure functions. Note that WVCs in the outer swath were not used in the processing to produce SeaWinds-KNMI.

Velocity increments are taken between members of each along-track sample after transforming wind vectors into components parallel (*La*) and perpendicular (*Ta*) to the satellite track, as indicated by the subscript *a*. The subscript *a* is retained throughout to remind the reader that the structure functions are for one-dimensional along-track cuts through the near-surface ocean wind field, whereas the theoretical relations in section 2 assume ensemble averages taken over all directions.

One could easily take samples in the cross-track direction to investigate anisotropic characteristics of the turbulence. We do not attempt that here for reasons that will become clear below.

Empirical velocity increment PDFs $P_r(\delta u_{La})$ and $P_r(\delta u_{Ta})$, where subscript r denotes lag r, were constructed using all $\delta u_{La}(r,t)$ and $\delta u_{Ta}(r,t)$ during a calendar month per region and per wind product. Structure functions were calculated after subtracting off the mean velocity increment

Table 1. Study Regions[a]

	West Pacific	Central Pacific	East Pacific
	140°E–180°E	180°E–220°E	220°E–260°E
North	WPN	CPN	EPN
5°N–10°N	(rainy)	(rainy)	(rainy)
Equatorial	WPE	CPE	EPE
5°S–5°N	(rainy)	(dry)	(dry)
South	WPS	CPS	EPS
10°S–5°S	(rainy)	(dry)	(dry)

[a]Geographical limits and nomenclature for the regions shown in Figure 2.

$$\delta U_{La}(r)=\sum_{\delta u_{La}} \delta u_{La} P_r(\delta u_{La}),$$
$$\delta U_{Ta}(r)=\sum_{\delta u_{Ta}} \delta u_{Ta} P_r(\delta u_{Ta}), \quad (10)$$

$$D_{LLa}(r)=\sum_{\delta u'_{La}} (\delta u'_{La})^2 P_r(\delta u'_{La}),$$
$$D_{TTa}(r)=\sum_{\delta u'_{Ta}} (\delta u'_{Ta})^2 P_r(\delta u'_{Ta}), \quad (11)$$

where $\delta u'_{La}(r)=\delta u_{La}(r)-\delta U_{La}(r)$ and $\delta u'_{Ta}(r)=\delta u_{Ta}(r)-\delta U_{Ta}(r)$.

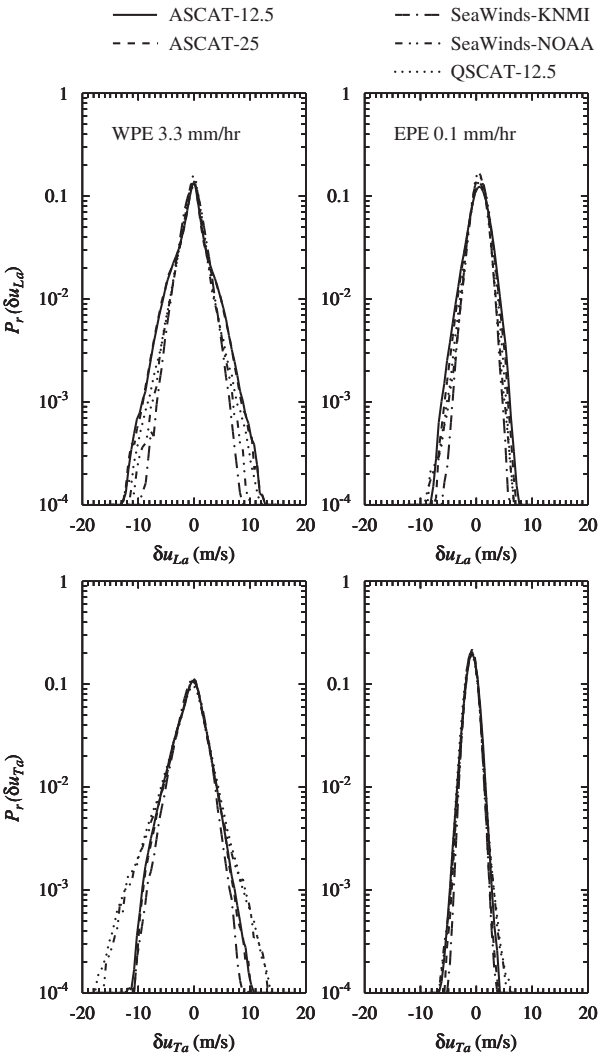

Figure 4. Longitudinal and transverse probability distributions for the equatorial regions in the west and east Pacific (July 2009): (top) $P_r(\delta u_{La})$ and (bottom) $P_r(\delta u_{Ta})$; (left) WPE and (right) EPE. July area-averaged SRAD rain-rate for WPE is 3.3 mm/hr and for EPE is 0.1 mm/hr.

4.4. Accuracy

Vogelzang et al. [2011] show that the scatterometer zonal and meridional wind components, u and v, have an accuracy of about 0.7 m/s (at the 1-σ level). The same accuracy holds for the along and cross-track components, u_L and u_T, so $\Delta u_L = \Delta u_T \approx 0.7$ m/s. The error variance in the differences δu_{La} and δu_{Ta} is estimated twice as large, so $\Delta(\delta u_{La}) = \Delta(\delta u_{Ta}) \approx 1.0$ m/s. The error in the square of the velocity increment is that value squared, so $\Delta(\delta u_{La})^2 = \Delta(\delta u_{Ta})^2 \approx 1.0$ m^2/s^2. Finally, the error in the second-order structure functions is $\Delta D_{LLa} = \Delta D_{TTa} \approx 1.0 N^{-1/2}$ m^2/s^2, with N the number of differences averaged over.

The value of N differs per lag, per region, and per wind product. Typically, N decreases as r increases. The equatorial longitude bands are twice as large as the Northern and Southern bands. ASCAT-12.5 has half the grid size as the other products, so it has four times as many points in a given region and a given period.

For lag size 1 and July 2009, the value of N ranges from 729,249 (ASCAT-12.5 in EPE) to 61,811 (ASCAT-25 in WPS), so ΔD_{LLa} and ΔD_{TTa} range from 0.001 to 0.004 m^2/s^2. For a range of 300 km, the value of N ranges from 529,290 (ASCAT-12.5 in EPE) to 22,574 (ASCAT-25 in WPS), so ΔD_{LLa} and ΔD_{TTa} range from 0.001 to 0.007 m^2/s^2. It is therefore safe to say that the errors in the results shown in the next section are negligible with respect to the scale of the figures, except for the last points at the highest lags.

The above error estimates are for directly calculated structure functions, whereas the results presented in this paper are calculated according to (10) and (11) and thus contain binning errors. However, the errors in the directly calculated structure functions are negligible (look ahead to Figure 5), so the accuracy of the results of (10) and (11) can be estimated by comparing with directly calculated structure functions. This shows that the results are accurate up to a few percent.

5. Results

5.1. Velocity Increment PDFs

By definition, the second-order structure function is the variance of velocity increments; that is, they measure the width of the velocity increment PDF. Therefore, it is instructive to begin by comparing some PDFs. Figure 4 shows semilog plots of the longitudinal and transverse PDFs $P_r(\delta u_{La})$ (top) and $P_r(\delta u_{Ta})$ (bottom) for July 2009 at scale $r = 200$ km. The plots on the left are for WPE, a rainy region, and the plots on the right for EPE, a dry region. There are five curves in each panel, one for each wind product, constructed from

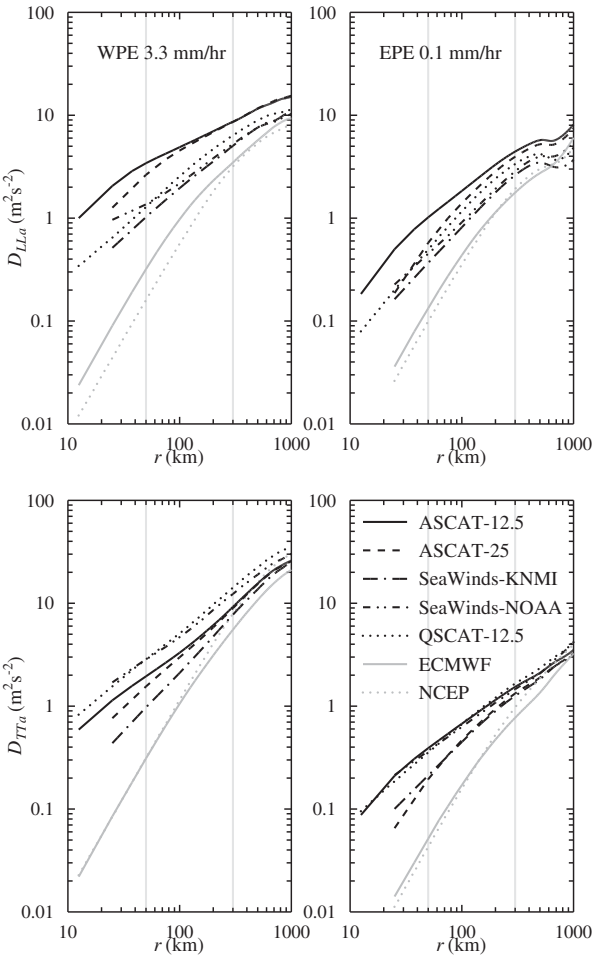

Figure 5. Structure functions for the equatorial regions in the west and east Pacific in July: (left) WPE and (right) EPE, (top) longitudinal, and (bottom) transverse. Vertical lines are drawn at 50 and 300 km, the range used to compare structure functions.

between 10^5 (SeaWinds-KNMI) and 10^6 (QSCAT-12.5) velocity increments. The figure shows that PDFs are wider in WPE than in EPE. This is because convergence, divergence, and vorticity are more energetic in WPE due to strong convective activity over warm SST, whereas in EPE the opposite holds because cool SST suppresses convective activity. It can also be seen that SeaWinds-KNMI PDFs are always narrower than SeaWinds-NOAA. This is because the SeaWinds-KNMI processing flags used here result in more wind retrievals as being of poor quality, thus producing narrower PDFs.

Comparing EPE PDFs (both longitudinal and transverse) across wind product shows only small differences between ASCAT and SeaWinds. In WPE, however, there are significant differences. SeaWinds has narrower longitudinal PDFs. Most likely this is due to the fact that when it rains, Ku-band systems see rain and not wind [*Weissman et al.*, 2012]. Since SeaWinds will not sample the wind as well in rainy areas its $P_r(\delta u_{La})$ will be narrower. QSCAT-12.5 and SeaWinds-NOAA have wider transverse PDFs. We cannot yet be sure why. The same is true in heavy rain months of all regions. This could be contributed by a diurnal effect, but unfortunately the satellite crossing times of MetOp-A and QuikSCAT are not spaced far enough apart to allow a definite conclusion one way or the other. Another possibility is that the SeaWinds PDFs contain contributions from unflagged rain contaminated wind retrievals. As discussed in section 3.4, the median filter used by SeaWinds can, in heavy rain, influence wind retrievals in neighboring rain-free WVCs. SeaWinds-KNMI, whose transverse PDFs are more in line with ASCAT, may be filtering out such contamination with its quality control. Further work is needed to be sure.

5.2. Structure Functions

Figure 5 shows how the widths of the PDFs (D_{LLa} and D_{TTa}) change with r for the WPE and EPE regions. Structure function slopes and magnitude (*TKE*) vary per wind product, per wind component, and per region. For reference, structure functions for the collocated ECMWF-12.5 and NCEP-12.5 winds are included in the figure. These have the steepest slopes and lowest *TKE*, dropping away from the scatterometer structure functions starting at about 500 km. This drop in *TKE* relative to scatterometer winds is well known from spectral studies (see Figure 2 in *Bourassa et al.* [2010]). It must be added that the difference is somewhat exaggerated by the fact that the interpolated ECMWF winds in the ASCAT wind products are generated from coarse model output (grid size about 60 km). The ASCAT wind products used here are operational near-real-time products generated since 2007, for which comparison with ECMWF predictions on this grid is part of the routine monitoring.

Figure 5 is partitioned into three ranges by vertical lines drawn at 50 and 300 km. For scales larger than 300 km, scatterometer and NWP structure functions are similar, while for scales $<$300 km scatterometer winds resolve more structure than NWP winds. Moreover, the 300 km and below range are the scales occupied by mesobeta scale weather phenomena such as squall lines and mesoscale convective systems [*Houze*,

2004]. At scales <50 km there are artifacts: ASCAT slopes steepen and SeaWinds-NOAA slopes flatten. The behavior of the ASCAT slopes at these scales is believed due to the spatial averaging carried out during EUMETSAT processing of the backscatter data. The flattening of the SeaWinds-NOAA slope is characteristic of noise [cf. *Vogelzang et al*., 2011]. It is also interesting to note that over the 50–300 km range, wind product structure functions do not cross each other. This means that if the PDFs were plotted at any r in that range, the resulting figure would look, after rescaling widths, just like Figure 4. Therefore, the best range of scales to make comparisons is the 50–300 km range.

Two features of the scatterometer structure functions in Figure 5 that are easy to identify are that their slopes vary and that they tend to fall into one of two groups based on their *TKE*. Closer inspection shows that in both regions the higher longitudinal *TKE* group is composed of ASCAT-12.5 and ASCAT-25, the higher transverse *TKE* group is composed of QSCAT-12.5 and SeaWinds-NOAA, and SeaWinds-KNMI always has the lowest *TKE*. Further inspection also shows that in EPE ASCAT-25 drops away from ASCAT-12.5 in both longitudinal and transverse *TKE*.

Remarks

i. The small SeaWinds-KNMI *TKE* is due to the stringent spatial filtering and quality control made necessary by the more complex SeaWinds ambiguity structure [*Portabella and Stoffelen*, 2006]. Even though the more stringent processing results in the smallest *TKE*, *Ebuchi* [2013] has found that this type of processing maintains excellent verification with 10 min mean moored buoy wind vectors for SeaWinds-type scatterometers.
ii. ASCAT-25 structure functions start to drop away from ASCAT-12.5 in both WPE and EPE. The reduction is consistent with the spectral analysis by *Vogelzang et al*. [2011], who traced the difference to the spatial aggregation of backscatter data. However, at present, we have no explanation for the difference in the scale at which *TKE* starts to drop: at 100 km in WPE and at 300 km in EPE.
iii. In EPE there is a significant gap in longitudinal *TKE* between ASCAT-12.5 and SeaWinds. Since EPE in July is dry, this cannot be attributed to rain contamination. One possible explanation is that it is a diurnal effect. Another possibility is that the reduced *TKE* results from the more complex spatial filtering required in SeaWinds processing.

In summary, the variability in structure function slopes and magnitudes shown in Figure 5 reflect differences in flow regime, instrument design, processing, and quality control. In addition to the variability already discussed, structure function characteristics vary seasonally. After inspecting structure functions for other months, we decided to compare the 1080 structure functions (five wind products, longitudinal and transverse components, nine regions, and 12 months), using the slopes and *TKE* at 300 km. As a check on the reasonableness of the results, we compare vorticity-to-divergence ratios.

5.3. Structure Function Slopes

Structure function slopes are estimated from straight-line fits over the 50–300 km range to D_{LLa} and D_{TTa} in log-log space. The longitudinal (β_{La}) and transverse slopes (β_{Ta}) are shown as a function of time in Figures 6 and 7, respectively. For reference, a horizontal line is drawn at the classical turbulence value 2/3. Error bars are drawn at plus minus 1 root-mean-square deviation. The error on each structure function value is small (section 4.4) and hence the root-mean-square error on each slope is really indicating how well the structure function follows a simple power law. The results indicate that structure functions are indeed well characterized by a power law whose value depends on region, season, instrument, and processing.

For each region, wind product time series are approximately parallel (more so for β_{La} than β_{Ta}), shifted vertically from one another by a significant amount. This can be seen more clearly in the scatter plots shown in Figure 8. In that figure, slopes β_{La} (top) and β_{Ta} (bottom) are referenced against those for ASCAT-12.5 (left) and QSCAT-12.5 (right). Slopes above (below) the diagonal are steeper (flatter) than the referenced slope.

First consider the scatter plots for β_{La}. The ASCAT intracomparison (top left) shows that ASCAT-25 is steeper than ASCAT-12.5 by roughly 0.2 everywhere. This is interesting since both products are processed by AWDP, with the main difference being the backscatter aggregation over respectively about 25 and 50 km—which appears to have a substantial effect on the slopes. On the other hand, the spatial characteristics of 2DVAR are different as well; and this could affect the flagging frequency. The SeaWinds intracomparison (top right) shows that SeaWinds-KNMI has steeper and SeaWinds-NOAA flatter slopes than QSCAT-12.5. This

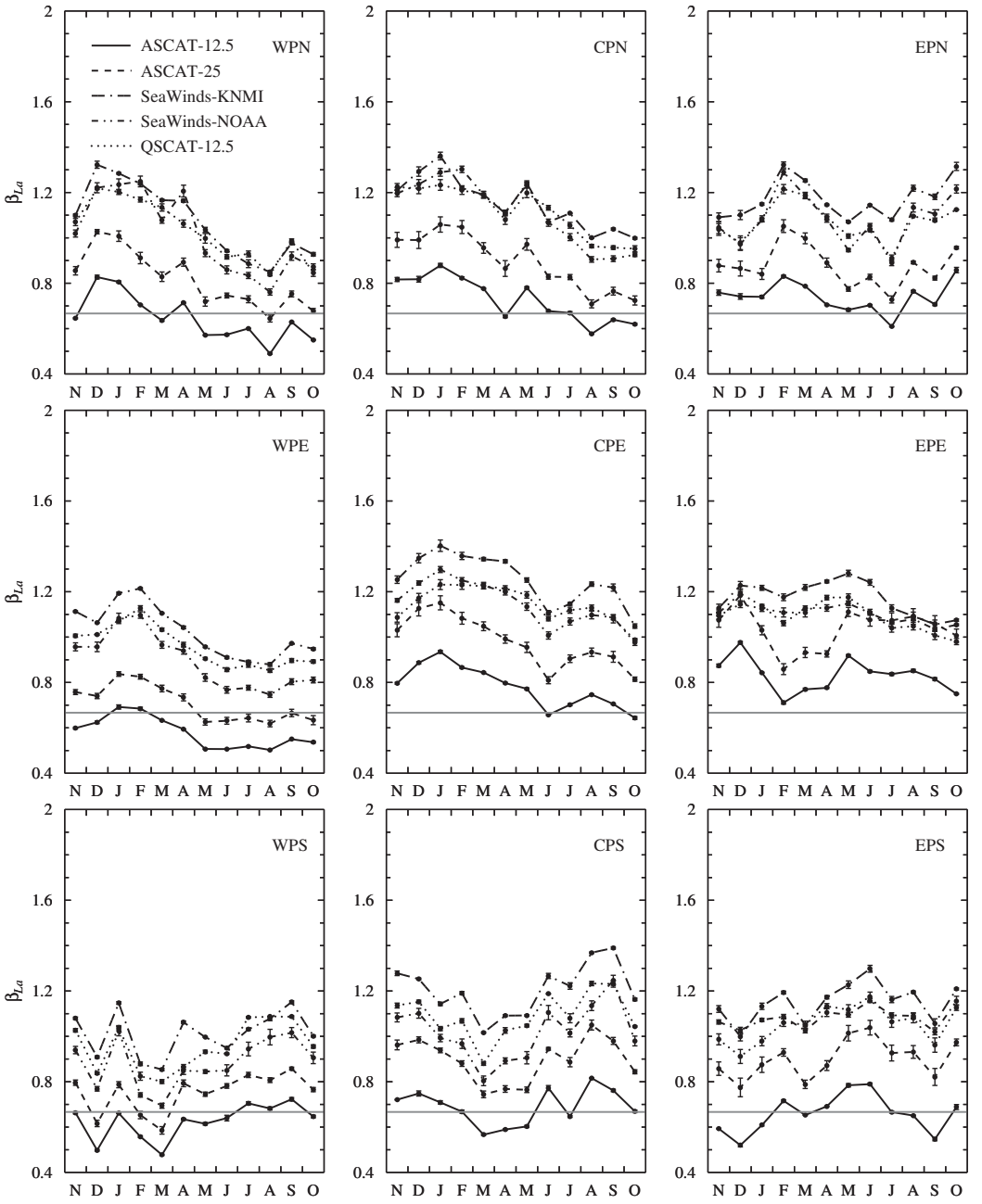

Figure 6. The longitudinal slope β_{La} as a function of time.

is not surprising. Finally, comparing QSCAT-12.5 and ASCAT-12.5 (top left) shows that QSCAT-12.5 is steeper by roughly 0.4 everywhere. The surprise here is that the difference is so large. The reason for this is not fully clear, but could be due to the constrained spatial filtering implied by the SeaWinds ambiguity removal. One final point to draw attention to is ASCAT-12.5 has the smallest longitudinal slopes, independent of region and month.

Next consider the scatter plots of β_{Ta}. The ASCAT intracomparison (bottom left) shows that for the transverse component ASCAT-25 is also steeper than ASCAT-12.5 by about 0.2 on average, but with a larger spread than for β_{La}. The SeaWinds intracomparison (bottom right) shows that SeaWinds-KNMI is steeper and SeaWinds-NOAA flatter than QSCAT-12.5. This is the same as for β_{La}, but it is interesting that SeaWinds-KNMI β_{Ta} is so much steeper than QSCAT-12.5 (by about 0.4) than for β_{La}. Finally, comparing QSCAT-12.5

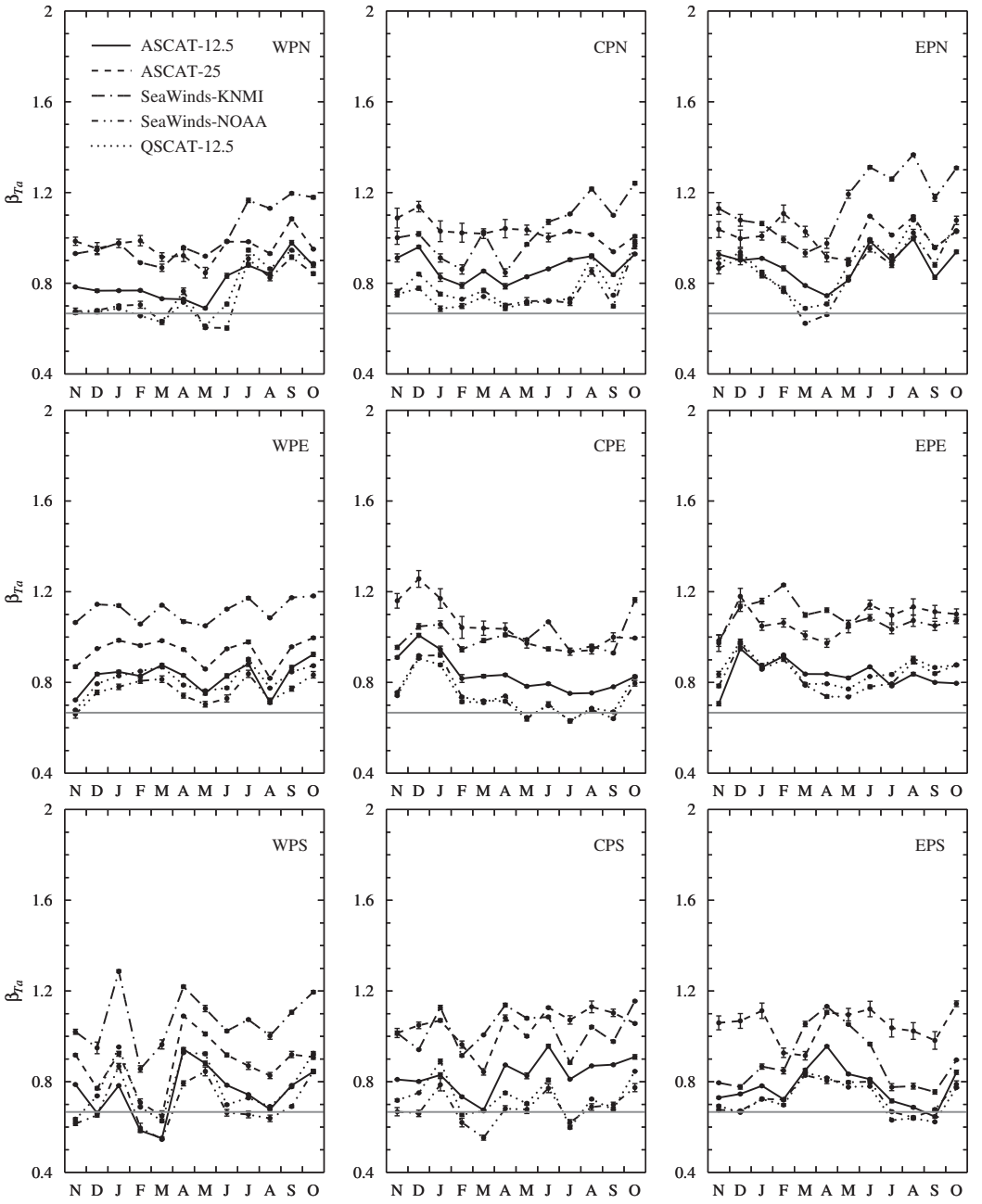

Figure 7. The transverse slope β_{Ta} as a function of time.

and ASCAT-12.5 (bottom left) shows that, in contrast to β_{La}, QSCAT-12.5 β_{Ta} are (mostly) flatter than ASCAT-12.5. We are unable to offer an explanation for this.

Another diagnostic is to plot β_{La} versus β_{Ta}. This is shown in Figure 9 for all ASCAT (left) and all SeaWinds (right). The diagonal line $\beta_{Ta}=\beta_{La}$ clearly identifies an interesting difference between ASCAT and SeaWinds slopes. Except for a few cases, ASCAT β_{Ta} is greater than β_{La}, while in the case of SeaWinds-NOAA and QSCAT-12.5, β_{Ta} is less than β_{La}. It is not clear why this is so. However, note that the results for SeaWinds-KNMI straddle the diagonal, indicating that in some cases the KNMI reprocessing of the NOAA product brings SeaWinds structure functions closer into agreement with ASCAT structure functions.

During our investigation, we found an interesting correlation between β_{La} and SST and plotted in Figure 10. In this figure, scatter plots of β_{La} versus SST are shown for ASCAT-12.5 (left) and QSCAT-12.5 (right). When

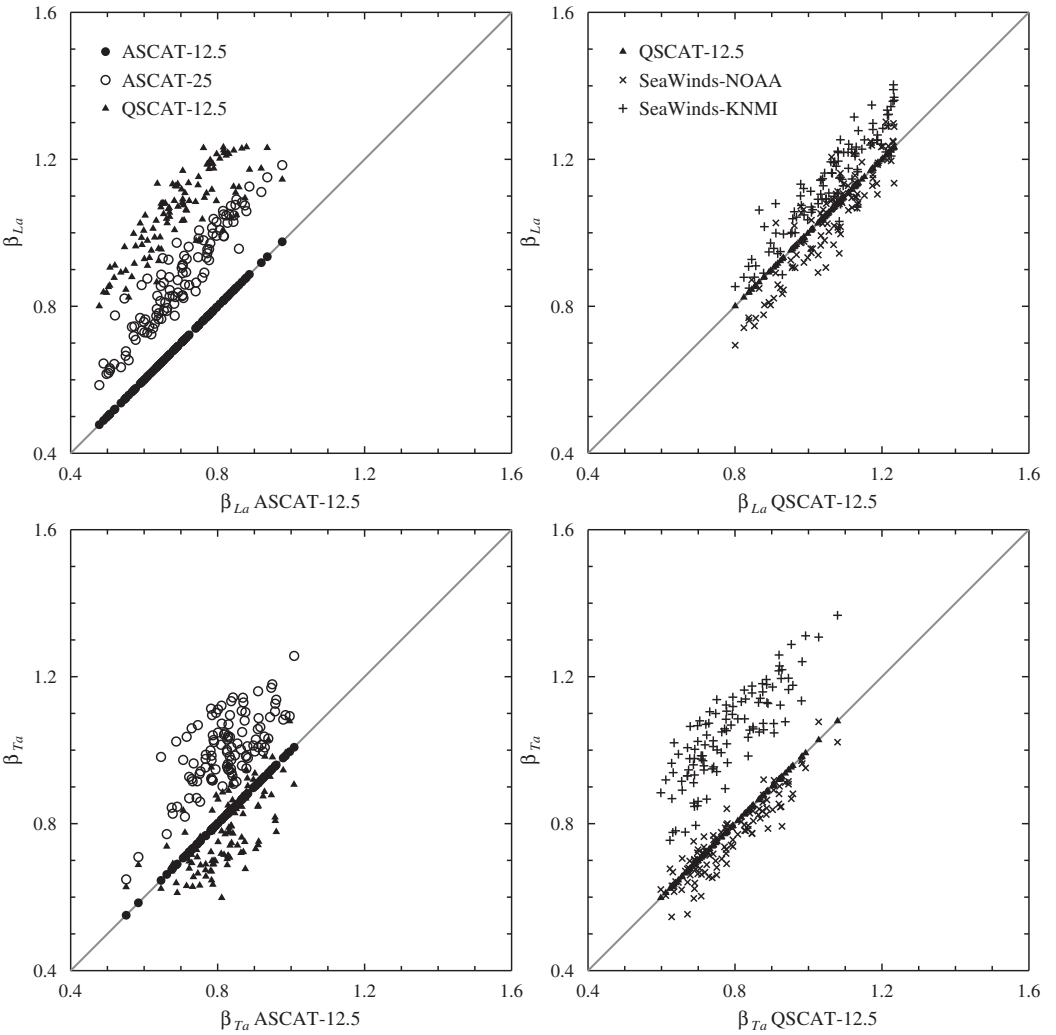

Figure 8. Scatter plots of all (top) β_{La} and (bottom) β_{Ta} referenced to those for (left) ASCAT-12.5 and (right) QSCAT-12.5 for the same month and region. Points above (below) the diagonal indicate slopes steeper (flatter) than the reference slope.

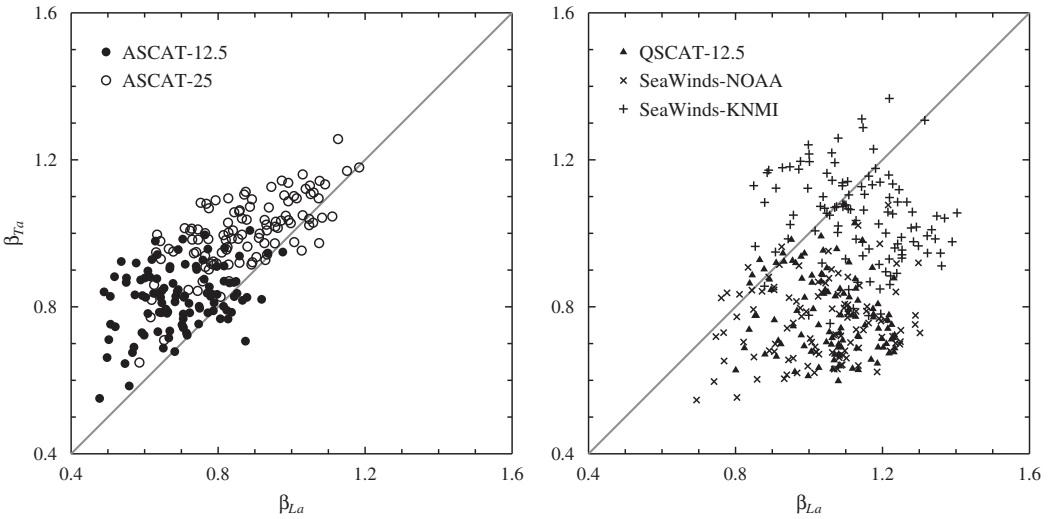

Figure 9. Scatter plots of β_{La} versus β_{Ta} for the same region and month: (left) ASCAT slopes and (right) SeaWinds. The diagonal line is where $\beta_{Ta}=\beta_{La}$.

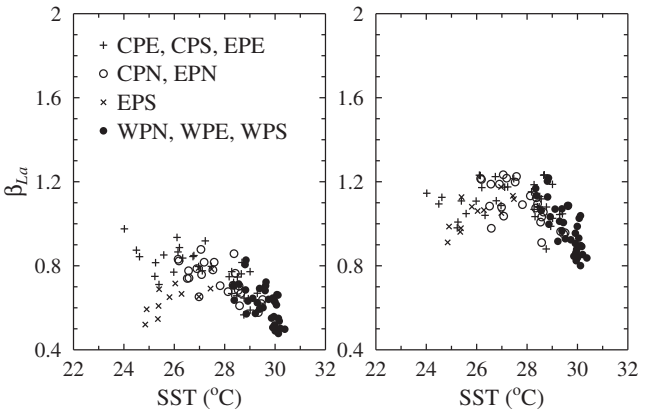

Figure 10. Scatter plots of β_{La} versus SST: (left) ASCAT-12.5 and (right) QSCAT-12.5.

SST exceeds the threshold for onset of deep convection (about 28°C), β_{La} rapidly falls in value. This implies the development of small-scale convergent (ascend) and divergent (downburst) features in the wind field.

β_{Ta} does not have a similar, easily identified signature as β_{La}. Figure 11 shows scatter plots of β_{Ta} versus SST; again only ASCAT-12.5 (left) and QSCAT-12.5 (right) are shown. Due to the complexity of the scatter plot, the equatorial region is plotted separately (top) from the combined northern and southern regions (bottom). In the equatorial regions, ASCAT slopes are independent of SST; however, QSCAT slopes show a decrease with SST similar to that shown for β_{La} in Figure 10 (right). The bottom plots show that as SST increases beyond 28°C, the distribution of β_{Ta} widens—ranging between about 0.6 up to about 1.1. The larger slopes occur in the tropical cyclone season of each hemisphere and hence are probably due to the propagation of tropical cyclones through the region and/or development of organized tropical convection.

5.4. Turbulent Kinetic Energy

An estimate of the turbulent kinetic energy *TKE* held in scales <300 km is given by $D_{jja}(r)$ at $r = 300$ km. This will be denoted by D^*_{jja}. Figure 12 shows D^*_{LLa} (divergent *TKE*) as a function of time in each region. The pattern of increasing and decreasing divergent *TKE* reflects the locations and seasonal migrations of the ITCZ, SPCZ, and S-ITCZ convergence zones (section 4.1). For example, in the northern regions, D^*_{LLa} increases as the ITCZ migrates north, and decreases as it migrates south. Also in EPS during the short time, the S-ITCZ appears (March/April), D^*_{LLa} rises to a peak. In all regions and in almost all months, ASCAT winds have largest and SeaWinds-KNMI smallest D^*_{LLa}.

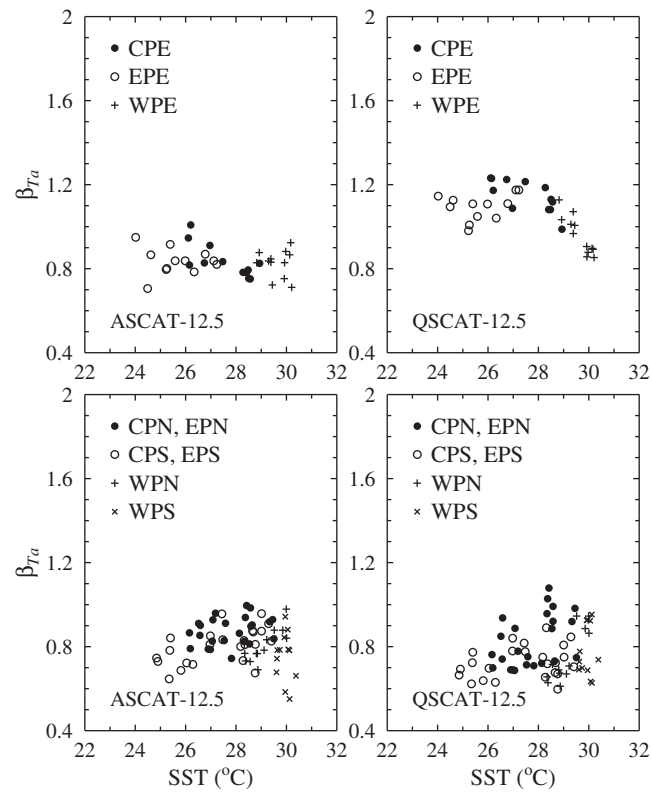

Figure 11. Scatter plots of β_{Ta} versus SST: (left) ASCAT-12.5 and (right) QSCAT-12.5; (top) equatorial region; (bottom) north and south regions.

Figure 13 shows D^*_{TTa} (vortical *TKE*) as a function of time in each region. In the northern regions, vortical *TKE* increases dramatically when the ITCZ is in a sufficiently northward position that the coriolis force amplifies background vorticity. This can be seen in WPN and CPN: a dramatic increase in D^*_{TTa} at the beginning of boreal summer (onset of the tropical cyclone season), and a drop in value at the end. In contrast to D^*_{LLa}, SeaWinds has larger values of D^*_{TTa} than ASCAT. In the rainy regions, the difference is very large during months

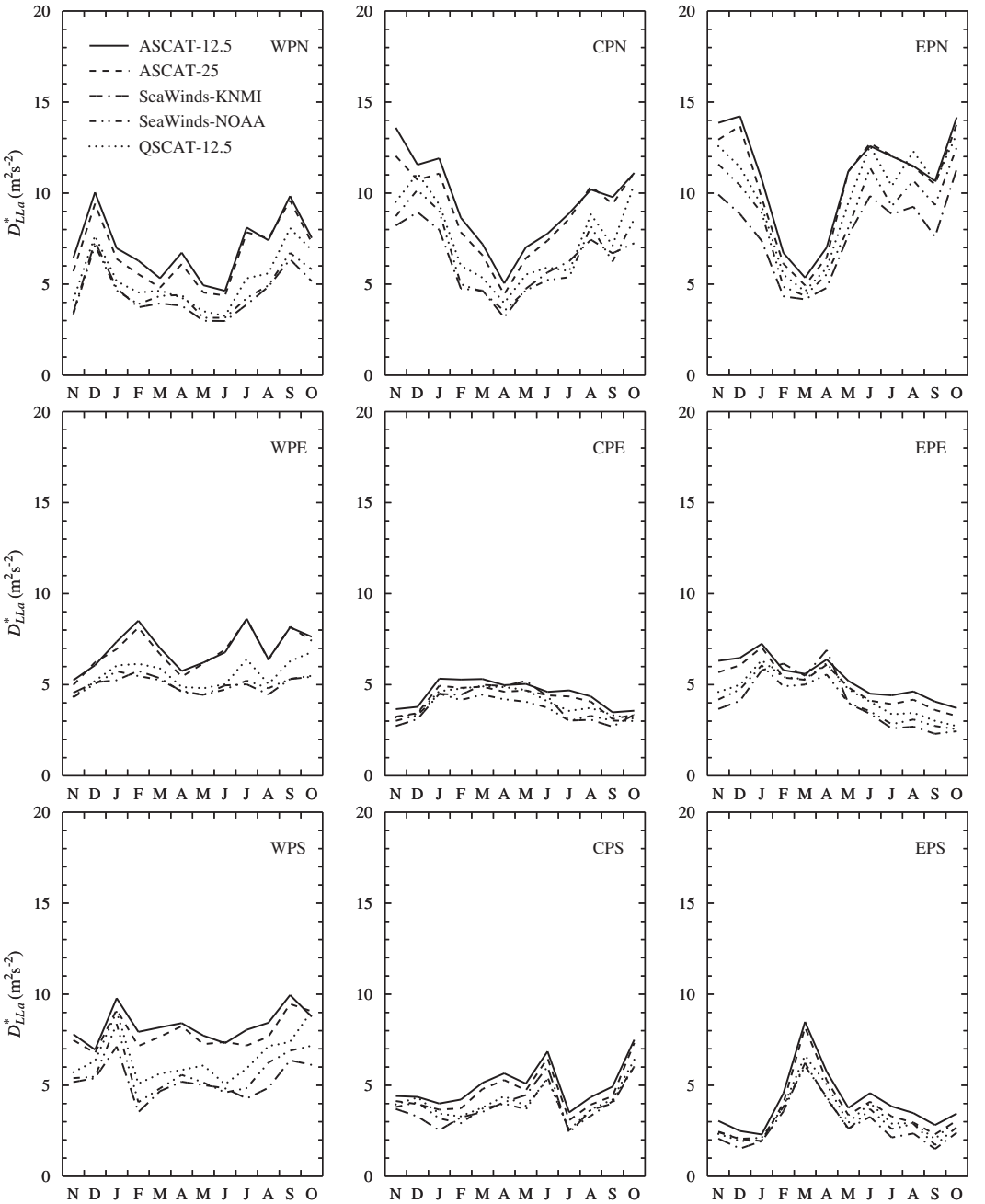

Figure 12. The longitudinal (divergent) turbulent kinetic energy D^*_{LLa} as a function of time.

when convective activity is strong. Strong convective activity implies rain and hence more artifacts in SeaWinds retrievals, suggesting that the larger values of D^*_{TTa} may be associated with rain artifacts. Lin et al. (submitted manuscript, 2014) verify ASCAT winds in rainy areas with buoys and find a clear wind signal in ASCAT. Unfortunately, such study has not been performed yet for QuikSCAT.

Figure 14 provides a summary of the *TKE* results in scatter plots of D^*_{LLa} (top) and D^*_{TTa} (bottom), referenced against ASCAT-12.5 (left) and QSCAT-12.5 (right). Points above (below) the diagonal line indicate more (less) *TKE* than the reference. Points in each figure spread out with increasing *TKE*. In the case of ASCAT intracomparisons (left plots), ASCAT-25 *TKE* is only slightly less than ASCAT-12.5. In the case of SeaWinds intracomparisons, SeaWinds-NOAA and SeaWinds-KNMI *TKE* are both less than QSCAT-12.5, but as *TKE* increases, the spread in SeaWinds-KNMI TKE is significantly larger than for SeaWinds-NOAA. The more interesting and

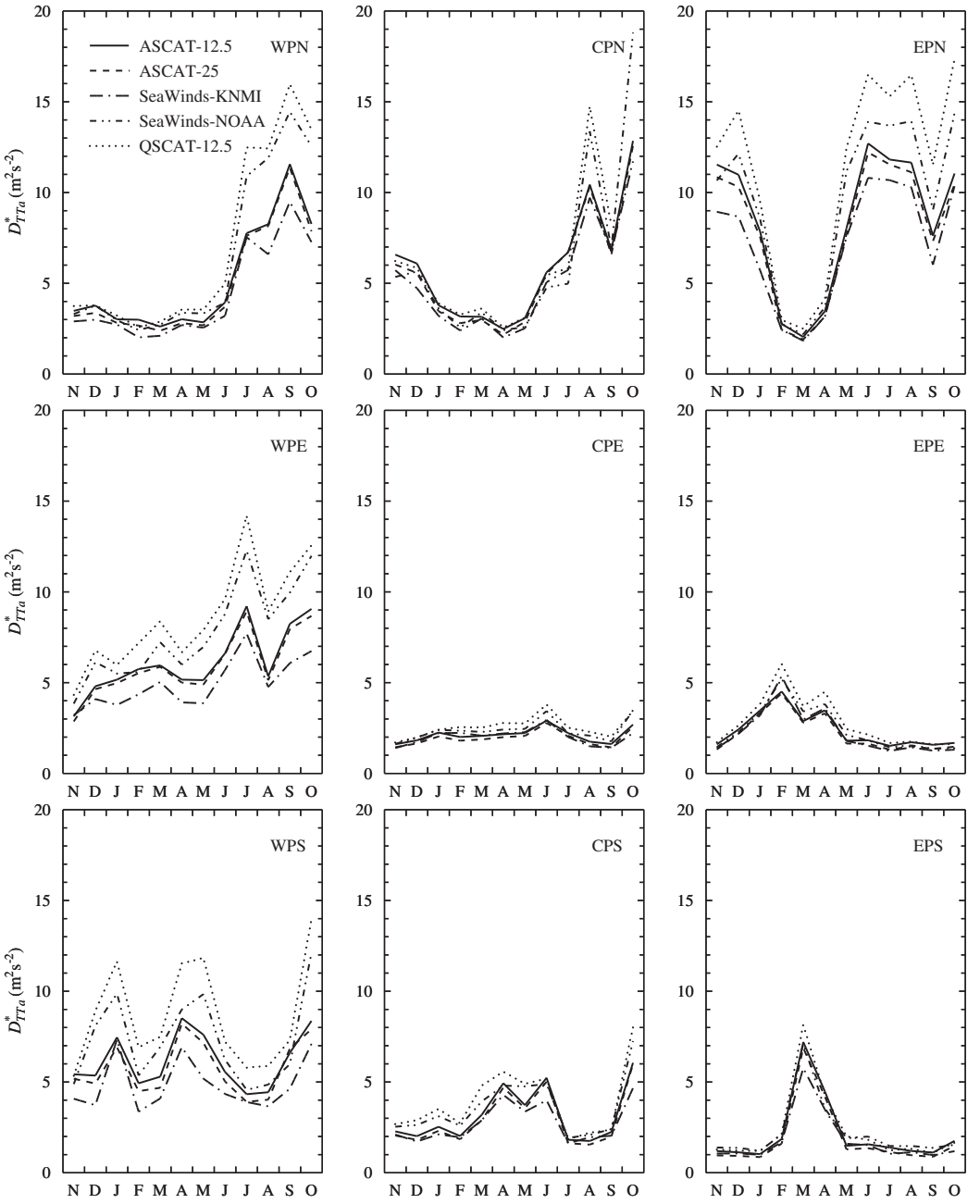

Figure 13. The transverse (shear or vortical) turbulent kinetic energy D^*_{TTa} as a function of time.

intriguing comparison is between QSCAT-12.5 and ASCAT-12.5. QSCAT-12.5 has less divergent *TKE* than ASCAT-12.5 (top left), but greater vortical *TKE* (bottom left). The latter may be associated with rain artifacts.

5.5. Vorticity-to-Divergence

The partitioning of energy between rotational and divergent motions is quantified by the vorticity-to-divergence ratio. Since we calculate structure functions using separations taken along only one direction, $R_a(r) = D_{TTa}(r)/D_{LLa}(r)$ cannot be compared directly with theory. Nevertheless, the averaging over many conditions implies that R_a should yield a qualitatively interesting measure of the ratio of vorticity-to-divergence.

Figure 15 shows a plot of $R_a(r)$ for regions WPE and EPE, and shows that R_a increases slowly with r. Because SeaWinds has larger vortical and smaller divergent *TKE*, it has larger vorticity-to-divergence than ASCAT. In

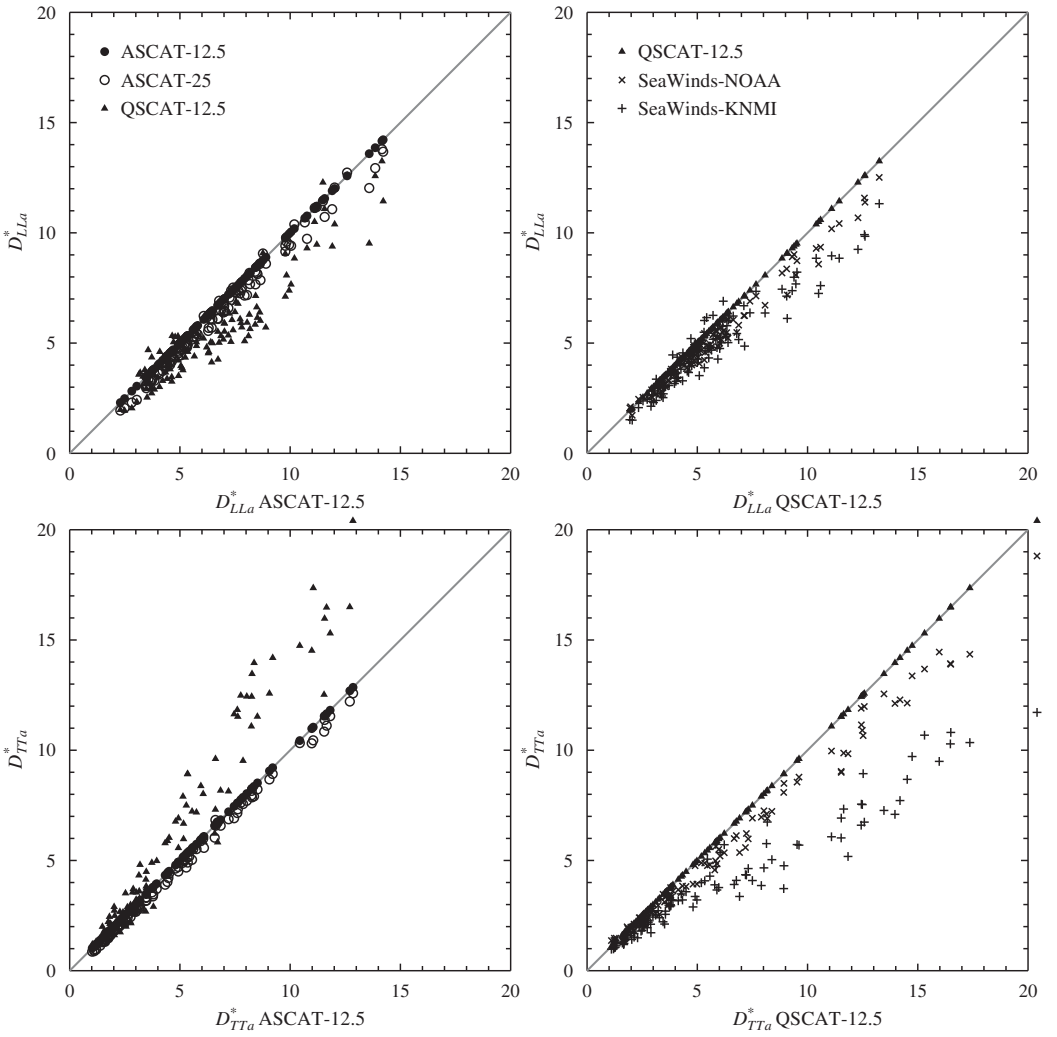

Figure 14. Scatter plots of all (top) D^*_{LLa} and (bottom) D^*_{TTa} referenced to those for (left) ASCAT-12.5 and (right) QSCAT-12.5 for the same month and region. Points above (below) the diagonal indicate more (less) turbulent kinetic energy than the reference.

order to explore the vorticity-to-divergence more conveniently across region and time, we graph $R^*_a = D^*_{TTa}/D^*_{LLa}$.

Figure 16 shows R^*_a as a function of time in each region. The horizontal line at $R^*_a = 1$ indicates where vortical and divergent *TKE* are equal. The key thing to note in this figure is that ASCAT and SeaWinds are in good qualitative agreement: vortical energy is enhanced over, or comparable to, divergent energy in the convectively active months of both the west and east Pacific, while the opposite is the case during the dry months in the dry regions. The difference between QSCAT-12.5 and ASCAT-12.5 in the rainy and especially the west Pacific regions is large—but is it too large? Recall from section 2.3 that turbulence theory predicts vorticity-to-divergence values ranging between 3/5 and 3. The graphs in Figure 16 show that R^*_a ranges between 0.4 and 2.5. Thus all wind products produce reasonable vorticity-to-divergence ratios, despite the noted effects related to rain artifacts, ambiguity, and spatial filtering.

6. Summary and Conclusions

Second-order along-track structure functions were calculated using wind products derived from radar backscatter measurements by ASCAT-on-MetOp-A and SeaWinds-on-QuikSCAT over the tropical Pacific (subdivided into rainy and dry regions) during the 12 month period November 2008 to October 2009. The wind products from each scatterometer were at two different grid spacings (12.5 and 25 km), and were derived using different processing and different quality control.

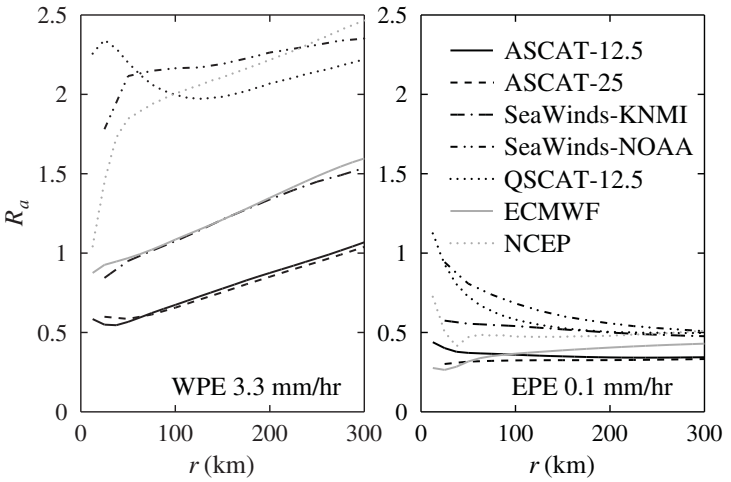

Figure 15. The ratio $R_a = D_{TTa}/D_{LLa}$ as a function of separation r for WPE and EPE in July 2009. The July area-averaged SRAD rain-rate for WPE is 3.3 mm h^{-1} and for EPE is 0.1 mm h^{-1}.

Longitudinal and transverse velocity increment PDFs and structure functions from along-track differences were used to illustrate and identify key differences between wind products. Detailed comparisons for all regions and months were made using structure function slopes, turbulent kinetic energy, and vorticity-to-divergence ratios estimated for the 50–300 km range of scales.

Qualitatively, results were in excellent agreement across wind product. All quantities from all wind products rose and fell together in each region, consistent with regional and seasonal dynamics. This gives confidence that the regionally and seasonally varying characteristics of turbulence are being identified correctly. An interesting correlation was found between the longitudinal structure function slopes and the monthly, area-averaged SST: when the mean SST exceeds about 28°C (the threshold for onset of deep convection), the longitudinal slope decreases rapidly (Figure 10), implying the development of small-scale convergent (ascend) and divergent (downburst) features in the wind field. The transverse slope showed a less clear connection with SST.

Quantitatively, results varied across wind product. The main difference between the two ASCAT products was that ASCAT-25 slopes were steeper than ASCAT-12.5 by about 0.2 everywhere (Figure 8). This is believed due to the backscatter aggregation, which is over about 50 and 25 km, respectively. Differences between the SeaWinds products were more and larger than between ASCAT products. This is not surprising since the processing and quality control used to produce these products differed. As expected, relative to QSCAT-12.5, SeaWinds-NOAA slopes were a little flatter and SeaWinds-KNMI slopes steeper—more so for transverse slopes (by about 0.3) than longitudinal slopes (about 0.1).

The main interest was in comparing ASCAT-12.5 and QSCAT-12.5, as these are the finest ASCAT and SeaWinds products. QSCAT-12.5 longitudinal slopes were found to be much steeper than ASCAT-12.5 (by about 0.4 everywhere), while the transverse slopes were typically a little flatter (by about 0.1). As spatial filtering has the effect of steepening the structure function, it is proposed that the reason for the steeper QSCAT-12.5 longitudinal slopes is the constrained spatial filtering implied by the more difficult SeaWinds ambiguity removal.

We recall the results of *Ebuchi* [2013], which for Oceansat-2 data reveal SeaWinds-KNMI as the better verifying product with local buoys, despite its 25 km WVC grid. Moreover, ASCAT-12.5 verifies better with buoys than any QuikSCAT product does [*Vogelzang et al.*, 2011]. However, these comparisons may not be conclusive and we conclude that at present it is difficult to identify a universal scaling exponent for mesoscales turbulence in ocean winds using current scatterometer data. However, this does not mean that the data cannot be used to address fundamental questions on turbulence in the atmosphere. As we have shown in a companion to this paper, third-order statistics from these same wind products can be used to identify the direction of the energy cascade [*King et al.*, 2015].

Comparison of *TKE* showed striking differences between QSCAT-12.5 and ASCAT-12.5. Differences increased with increasing *TKE*. Two possible reasons for this were already mentioned when discussing the PDFs. One is that the difference is real and related to diurnal effects. This possibility can be assessed when data from the recently launched RapidSCAT mission becomes available. A second possibility is that the difference is a result of the sensitivity of Ku-band radar to rain. For example, it is known that rain can give rise to artificial strong zonal winds in SeaWinds wind retrievals [*Chelton and Freilich*, 2005; *Hoffman and Leidner*, 2005]. For

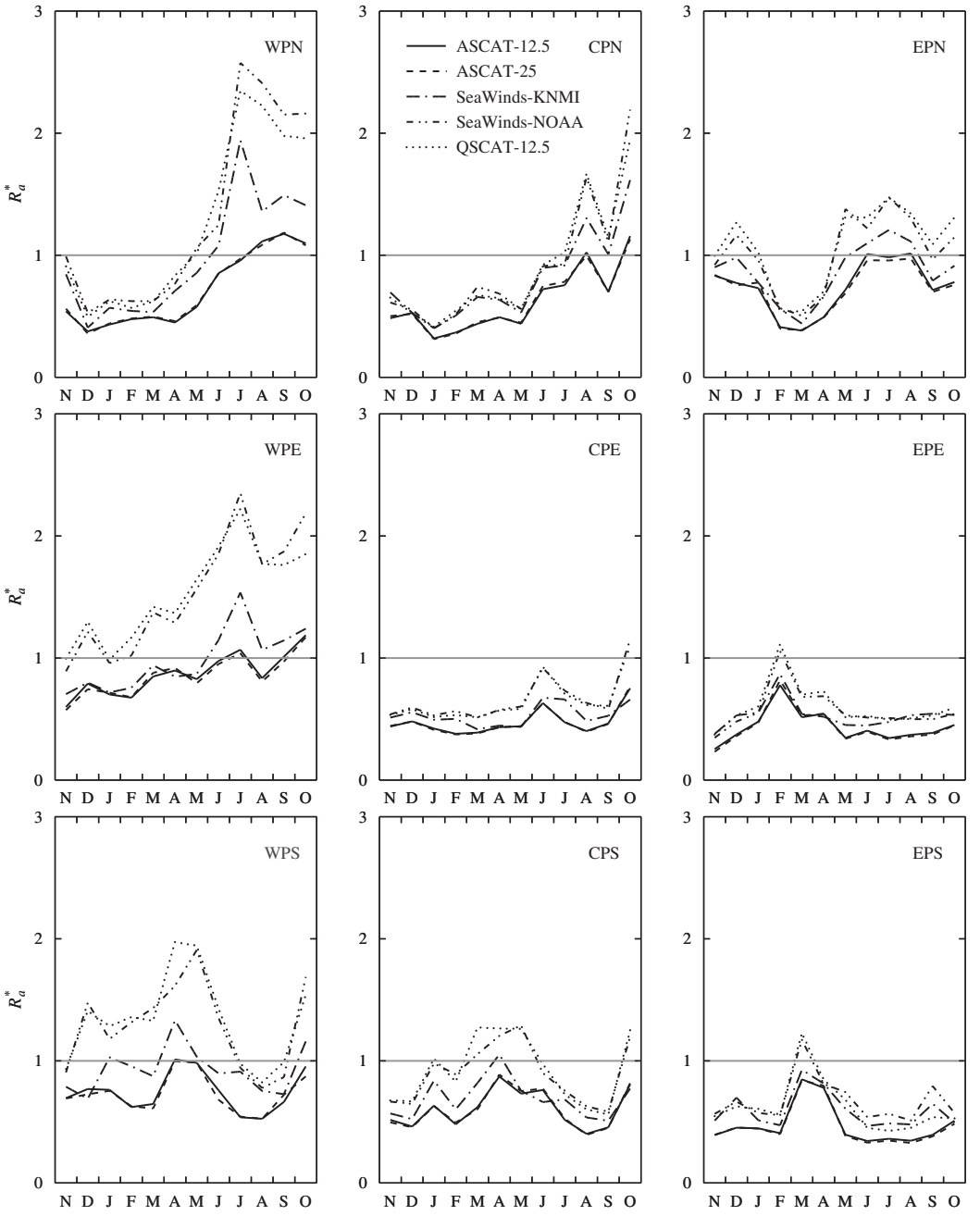

Figure 16. Time series of $R_a^* = D_{TTa}^* / D_{LLa}^*$, a measure of the ratio of vorticity-to-divergence.

the along-swath track analysis in this paper, this results in an additional contribution to the transverse component of the structure functions and hence wider transverse PDF and larger transverse *TKE*.

The work reported here has shown that structure functions allow a detailed investigation and comparison of regional winds. In future, it would be valuable to apply these methods to study isolated synoptic cases and learn their signatures (e.g., mesoscale convective systems, the Madden-Julian Oscillation, tropical cyclones, etc.), and to investigate ocean winds in regions of special interest (e.g., Indian Ocean, Kuroshio, Gulf Stream, Southern Ocean, etc.).

In closing, we emphasize that the differences between ASCAT-12.5 and QSCAT-12.5 bring up the same questions: are the differences in results due to diurnal variations, or are they due to unflagged rain-contamination? Further work is needed to resolve this.

Acknowledgments
The ASCAT-12.5 and ASCAT-25 data used in this work can be ordered online from the EUMETSAT Data Centre (www.eumetsat.int) as SAF type data in BUFR or NetCDF format. They can also be ordered from PO.DAAC (podaac.jpl.nasa.gov) in NetCDF format only. The SeaWinds-NOAA and QuikSCAT-12.5 data are also available from PO.DAAC. The SeaWinds-KNMI data are available from the KNMI archive upon an email request to scat@knmi.nl. Rain-rates and sea surface temperatures were obtained from the Tropical Rainfall Measuring Mission's (TRMM) Microwave Imager (TMI) archive at the Remote Sensing Systems web site (www.ssmi.com). SeaWinds Radiometer (SRAD) rain-rates were obtained from the QuikSCAT 25 km L2B science data product that is available from PO.DAAC. This work has been funded by EUMETSAT in the context of the Numerical Weather Prediction Satellite Applications Facility (NWP SAF). The contribution of GPK has been supported by EUMETSAT as part of the SAF Visiting Scientists programme. The authors thank Bryan Stiles, Robert Kerr, Mark Brend, Changming Dong, Richard Scott, and David Dritschel for helpful comments. We also thank the anonymous Reviewers for their comments and criticisms which greatly helped us improve the manuscript.

References

Bourassa, M., et al. (2010), "Remotely Sensed Winds and Wind Stresses for Marine Forecasting and Ocean Modeling" in *Proceedings of OceanObs'09: Sustained Ocean Observations and Information for Society* (vol. 2), 21–25 September 2009, edited by J. Hall, D. E. Harrison, and D. Stammer, ESA Publication WPP-306, Venice, Italy, doi:10.5270/OceanObs09.cwp.08.

Chelton, D. B., and M. H. Freilich (2005), Scatterometer-based assessment of 10-m wind analyses from the operational ECMWF and NCEP Numerical Weather Prediction models, *Mon. Weather Rev.*, *133*, 409–429.

Draper, D. W., and D. G. Long (2002), An assessment of SeaWinds on QuikSCAT wind retrieval, *J. Geophys. Res.*, *107*(C12), 3212, doi:10.1029/2002JC001330.

Dunbar, R. S., et al. (2006), *QuikSCAT Science Data Product User's Manual*, Jet Propul. Lab., Pasadena, Calif.

Ebuchi, N. (2013), Intercomparison of four ocean vector wind products from OCEANSAT-2 scatterometer, in *International Ocean Vector Winds Science Team Meeting*, Centre for Ocean-Atmospheric Prediction Studies (COAPS), Florida State University, Tallahassee, USA. [Available at http://coaps.fsu.edu/scatterometry/meeting/docs/2013/First%20Results/Ebuchi_IOVWST2013.pdf.]

Figa-Saldaña, J., J. Wilson, E. Attema, R. Gelsthorpe, M. Drinkwater, and A. Stoffelen (2002), The advanced scatterometer (ASCAT) on the meteorological operational (MetOp) platform: A follow on for the European wind scatterometers, *Can. J. Remote Sens.*, *28*, 404–412, doi:10.5589/m02-035.

Fore, A., B. Stiles, A. Chau, B. Williams, R. Dunbar, and E. Rodríguez (2013), Point-wise wind retrieval and ambiguity removal improvements for the QuikSCAT climatological data set, *IEEE Trans. Geosci. Remote Sens.*, *99*, 1–9, doi:10.1109/TGRS.2012.2235843.

Frehlich, R., and R. Sharman (2010), Climatology of velocity and temperature turbulence statistics determined from Rawinsonde and ACARS/AMDAR data, *J. Appl. Meteorol. Climatol.*, *49*, 1149–1169, doi:10.1175/2010JAMC2196.1.

Freilich, M. H., and D. B. Chelton (1986), Wavenumber spectra of Pacific winds measured by the Seasat scatterometer, *J. Phys. Oceanogr.*, *16*, 751–757.

Frisch, U. (1995), *Turbulence: The Legacy of A. N. Kolmogorov*, Cambridge Univ. Press, Cambridge, U. K.

Hoffman, R. N., and S. M. Leidner (2005), An introduction to the near-real-time QuikSCAT data, *Weather Forecasting*, *20*, 476–493, doi:10.1175/WAF841.1.

Houze, R. A. (2004), Mesoscale convective systems, *Rev. Geophys.*, *42*, RG4003, doi:10.1029/2004RG000150.

Isaksen, L., and P. A. E. M. Janssen (2004), Impact of ERS scatterometer winds in ECMWF's assimilation system, *Q. J. R. Meteorol. Soc.*, *130*, 1793–1814, doi:10.1256/qj.03.110.

King, G. P., J. Vogelzang, and A. Stoffelen (2015), Upscale and downscale energy transfer over the tropical Pacific revealed by scatterometer winds, *J. Geophys. Res. Oceans*, *120*, doi:10.1002/JC009993.

KNMI (2006), SeaWinds Product Manual, EUMETSAT OSI SAF report SAF/OSI/KNMI/TEC/MA/134, KNMI, De Bilt, Netherlands. [Available at www.knmi.nl/scatterometer.]

KNMI (2013), ASCAT Wind Product User Manual, EUMETSAT OSI SAF report SAF/OSI/CDOP/KNMI/TEC/MA/126, KNMI, De Bilt, Netherlands. [Available at www.knmi.nl/scatterometer.]

Kolmogorov, A. N. (1941), The local structure of turbulence in incompressible viscous fluid for very large Reynolds numbers, *Dokl. Akad. Nauk SSSR*, *30*, 299–303. Reprinted in the *R. Soc. London*, *434*, 9–13; *Proc. R. Soc. London, Ser. A*, *434*, 9–13 [1991].

Lander, M. A. (1996), Specific tropical cyclone track types and unusual tropical cyclone motions associated with a reverse-oriented monsoon trough in the western North Pacific, *Weather Forecasting*, *11*(2), 170–186, doi:10.1175/1520-0434(1996)011<0170:STCTTA>2.0.CO;2.

Laupattarakasem, P., W. Jones, K. Ahmad, and S. Veleva (2005), Calibration/validation of the SeaWinds radiometer rain rate algorithm, in *OCEANS, 2005. Proceedings of MTS/IEEE*, vol. 3, pp. 2601–2604, IEEE, N. Y., doi:10.1109/OCEANS.2005.1640163.

Lindborg, E. (1999), Can the atmospheric kinetic energy spectrum be explained by two-dimensional turbulence?, *J. Fluid Mech.*, *388*, 259–288, doi:10.1017/S0022112099004851.

Lindborg, E. (2007), Horizontal wavenumber spectra of vertical vorticity and horizontal divergence in the upper troposphere and lower stratosphere, *J. Atmos. Sci.*, *64*(3), 1017–1025, doi:10.1175/JAS3864.1.

Liu, W. T. (2002), Progress in scatterometer application, *J. Oceanogr.*, *58*, 121–136.

Masunaga, H., and T. S. L'Ecuyer (2010), The southeast Pacific warm band and double ITCZ, *J. Clim.*, *23*, 1189–1208, doi:10.1175/2009JCLI3124.1.

Mitchell, T. P., and J. M. Wallace (1992), The annual cycle in equatorial convection and sea surface temperature, *J. Clim.*, *5*, 1140–1156.

Nastrom, G. D., K. S. Gage, and W. H. Jasperson (1984), Kinetic energy spectrum of large-and mesoscale atmospheric processes, *Nature*, *310*, 36–38, doi:10.1038/310036a0.

Patoux, J., and R. A. Brown (2001), Spectral analysis of QuikSCAT surface winds and two-dimensional turbulence, *J. Geophys. Res.*, *106*(D20), 23,995–24,005, doi:10.1029/2000JD000027.

Portabella, M., and A. Stoffelen (2002), A comparison of KNMI quality control and JPL rain flag for SeaWinds, *Can. J. Remote Sens.*, *28*, 424–430.

Portabella, M., and A. Stoffelen (2004), A probabilistic approach for SeaWinds data assimilation, *Q. J. R. Meteorol. Soc.*, *130*(596), 127–159, doi:10.1256/qj.02.205.

Portabella, M., and A. Stoffelen (2006), Scatterometer backscatter uncertainty due to wind variability, *IEEE Trans. Geosci. Remote Sens.*, *44*, 3356–3362, doi:10.1109/TGRS.2006.877952.

Portabella, M., and A. C. M. Stoffelen (2009), On scatterometer ocean stress, *J. Atmos. Oceanic Technol.*, *26*(2), 368–382, doi:10.1175/2008JTECHO578.1.

Portabella, M., A. Stoffelen, W. Lin, A. Turiel, A. Verhoef, J. Verspeek, and J. Ballabrera-Poy (2012), Rain effects on ASCAT retrieved winds: Towards an improved quality control, *IEEE Trans. Geosci. Remote Sens.*, *50*, 2495–2506, doi:10.1109/TGRS.2012.2185933.

Sienkiewicz, J., M. J. Brennan, R. Knabb, P. S. Chang, H. Cobb, Z. J. Jelenak, K. A. Ahmad, S. Soisuvarn, D. Kosier, and G. Bancroft (2010), Impact of the loss of QuikSCAT on NOAA MWS marine warning and forecast operations, in *First International Ocean Vector Winds Science Team Meeting*. [Available at http://coaps.fsu.edu/scatterometry/meeting/past.php#2010_may.]

Sreenivasan, K., and R. Antonia (1997), The phenomenology of small-scale turbulence, *Annu. Rev. Fluid Mech.*, *29*, 435–472, doi:10.1146/annurev.fl.23.010191.002543.

Stiles, B., B. Pollard, and R. Dunbar (2002), Direction interval retrieval with thresholded nudging: A method for improving the accuracy of QuikSCAT winds, *IEEE Trans. Geosci. Remote Sens.*, *40*, 79–89, doi:10.1109/36.981351.

Stoffelen, A., and M. Portabella (2006), On Bayesian scatterometer wind inversion, *IEEE Trans. Geosci. Remote Sens.*, *44*(6), 1523–1533, doi:10.1109/TGRS.2005.862502.

Stoffelen, A., S. de Haan, Y. Quilfen, and H. Schyberg (2000), ERS scatterometer ambiguity removal scheme comparison, Technical Note EUMETSAT Ocean and Sea Ice SAF, KNMI, De Bilt, Netherlands. [Available at http://www.knmi.nl/publications/fulltexts/safosi_w_arcomparison.pdf.]

Stoffelen, A., M. Portabella, A. Verhoef, J. Verspeek, and J. Vogelzang (2008), Advancements in scatterometer wind processing, in 9th International Winds Workshop (9IWW), EUMETSAT, Darmstadt, Germany. [Available at http://www.eumetsat.int/website/wcm/idc/idcplg?IdcService=GET_FILE&dDocName=PDF_CONF_P51_S7_34_STOFFELE_V&RevisionSelectionMethod=LatestReleased&Rendition=Web.]

Tsai, W.-T., M. Spencer, C. Wu, C. Winn, and K. Kellogg (2000), SeaWinds on QuikSCAT: Sensor description and mission overview, International Geoscience and Remote Sensing Symposium 2000, in Proceedings IGARSS 2000, vol. 3, pp. 1021–1023, IEEE 2000 International, doi:10.1109/IGARSS.2000.858008.

Verhoef, A., and A. Stoffelen (2013), ASCAT coastal winds validation report, EUMETSAT OSI SAF Technical note SAF/OSI/CDOP/KNMI/TEC/RP/176, KNMI, De Bilt, Netherlands. [Available at http://www.knmi.nl/scatterometer/publications/pdf/ASCAT_validation_coa.pdf.]

Vogelzang, J., A. Stoffelen, A. Verhoef, J. de Vries, and H. Bonekamp (2009), Validation of two-dimensional variational ambiguity removal on SeaWinds scatterometer data, *J. Atmos. Oceanic Technol.*, *26*, 1229–1245, doi:10.1175/2008JTECHA1232.1.

Vogelzang, J., A. Stoffelen, A. Verhoef, and J. Figa-Saldaña (2011), On the quality of high-resolution scatterometer winds, *J. Geophys. Res.*, *116*, C10033, doi:10.1029/2010JC006640.

Weissman, D. E., B. W. Stiles, S. M. Hristova-Veleva, D. G. Long, D. K. Smith, K. A. Hilburn, and W. L. Jones (2012), Challenges to satellite sensors of ocean winds: Addressing precipitation effects *J. Atmos. Oceanic Technol.*, *29*, 356–374, doi:10.1175/JTECH-D-11-00054.1.

Wikle, C. K., R. F. Milliff, and W. G. Large (1999), Surface wind variability on spatial scales from 1 to 1000 km observed during TOGA COARE, *J. Atmos. Sci.*, *56*, 2222–2231.

Wyrtki, K. (1989), Some thoughts about the west Pacific warm pool, in *Proceedings of the Western Pacific International Meeting and Workshop on TOGA COARE*, edited by J. Picaut, R. Lucas, and T. Delcroix, pp. 99–109, Office de la Recherche Scientifique et Tecnique d'Outre-Mer, Cent. de Nouma, New Caledonia.

Xu, Y., L.-L. Fu, and R. Tulloch (2011), The global characteristics of the wavenumber spectrum of ocean surface wind, *J. Phys. Oceanogr.*, *41*, 1576–1582, doi:10.1175/JPO-D-11-059.1.

Zhu, B., and B. Wang (1993), The 30–60-day convection seesaw between the tropical Indian and western Pacific Oceans, *J. Atmos. Sci.*, *50*, 184–199, doi:10.1175/1520-0469(1993)050<0184:TDCSBT>2.0.CO;2.